SOLUTE AND PRECIPITATE EFFECTS ON MAGNESIUM RECRYSTALLIZATION AND GRAIN GROWTH

by

Gillian K. Storey

A thesis submitted to the Faculty and the Board of Trustees of the Colorado School of Mines in partial fulfillment of the requirements for the degree of Master of Science (Metallurgical Engineering).

Golden, Colorado

Date _____

Signed: _____

Gillian K. Storey

Signed: _____

Dr. Kester D. Clarke
Thesis Advisor

Golden, Colorado

Date _____

Signed: _____

Dr. Ivar Reimanis
Professor and Department Head
Department of Metallurgical and Materials Engineering

ABSTRACT

Recrystallization and grain growth kinetics of magnesium alloys can vary significantly based upon precipitate and solute content. Rare earth alloying elements, such as Ce, have been shown to stabilize grain size at elevated temperatures and thereby improve elevated-temperature properties. Quantifying the effects of precipitate fraction and solute content can result in fundamental understanding that will enable optimized industrial processing pathways. The baseline composition for this study is ZK60. Several variations on ZK60 compositions with different Zn and Ce levels were evaluated, which result in variations in second phase insoluble particle type, solute distribution and volume fraction that have strong effects on both grain size and recrystallization. After cold rolling and static annealing heat treatments from 6-60h at 350-400°C, microstructural characterization and microhardness tests were conducted. These results provide insights into mechanical and microstructural characteristics, including hardness, grain size distribution and texture, which are affected by enhanced or retarded recrystallization and grain growth kinetics. Increases in precipitate and solute content increase Zener pinning and solute drag and decreases static recrystallization (SRX) and grain growth kinetics. Texture weakening occurs during SRX and dynamic recrystallization (DRX), while near-basal (0001) orientated grains grow preferentially during grain growth. Modeling of DRX processes is determined by calculations of the critical stress required for DRX initiation. Hot compression tests were carried out on these alloys from 350-400°C via the Gleeble 3500 thermomechanical simulator at various strain rates. Microstructural characterization provides further insights into grain size distribution and texture, which are enhanced or retarded by DRX kinetics. A constitutive model shows that increased strain and lower temperatures require greater stress input for DRX to occur. The flow curves exhibit work hardening, softening and steady states. Ce additions impede DRX kinetics to a greater extent than Zn additions. Texture weakening readily occurs and is observed in the post-DRX microstructures.

TABLE OF CONTENTS

LIST OF FIGURES

LIST OF TABLES

LIST OF SYMBOLS

Revolutions per minute . . . . . RPM

Vickers microhardness . . . . . HV

Zener Hollomon parameter . . . . . Z

activation energy . . . . . Q(kJ/mol)

gas constant . . . . . R (J/molK)

strain . . . . . ϵ

stress . . . . . σ(MPa)

stress exponent . . . . . n

temperature . . . . . T (°C/K)

LIST OF ABBREVIATIONS

Continuous dynamic recrystallization . . . . . $CDRX$

Dynamic recrystallization . . . . . DRX

Electron dispersive spectroscopy . . . . . EDS

Field Emission Scanning Electron Microscope . . . . . $FESEM$

Hexagonal close packed . . . . . HCP

Inverse pole figure . . . . . IPF

Neightbor Pattern Averaging Indexing . . . . . $NPAR$

Orientation Imaging Microscopy . . . . . OIM

Particle-simulated nucleation . . . . . PSN

Rare earth . . . . . RE

Scanning Electron Microscope . . . . . SEM

Stacking fault energy . . . . . SFE

Static recrystallization . . . . . SRX

The American Society for Testing and Materials . . . . . $ASTM$

Twin-induced nucleation . . . . . TIN

X-ray diffraction . . . . . XRD

ACKNOWLEDGMENTS

Without the support of the friends, family, professors, and students around me this work would not have been possible. First and foremeost, I would like to thank my advisor Dr. Kester Clarke for continued support during this M.S. project, for his valuable insight, knowledge and encouragement.

I would also like to thank committee members, Dr. Amy Clarke and Dr. Emmanuel De Moor, for helpful advice, informed commentary and questioning.

My sincerest thanks goes to all graduate students in the Center for Advanced Non-Ferrous Structural Alloys (CANFSA), fellow labmates and officemates for informed discussions and support. Special thanks as well goes to Scott Sutton and Dan Hartman from Mag Specialties Inc. for supplying all material studied during this project and for all valuable insights along the way.

Last but especially not least, I would like to thank my family, significant other and friends for all of their emotional support and interest in my studies over the years.

Also to note: This work was conducted within the NSF I/UCRC Center for Advanced Non-Ferrous Structural Alloys(CANFSA) which is a joint industry-university collaborative research center between the Colorado School of Mines and Iowa State University. Mag Specialties, Inc. supplied and designed all alloys evaluated during the project duration.

CHAPTER 1
INTRODUCTION

This project investigates the effect of varying precipitate and solute content in Mg-Zn-Ce alloys on recrystallization and grain growth kinetics. The composition experimental matrix is divided by 3 levels of Zn (1.4-6.8 wt%), varying the hypothesized solute volume, and 3 levels of cerium addition (0.12-0.38 wt%), varying the hypothesized precipitate volume fraction. The effect of Ce microalloying with Zn additions on static recrystallization (SRX), dynamic recrystallization (DRX) and grain growth kinetics is examined. The texture evolution through each process and resulting physical properties are evaluated. This project can be effectively be split into 2 sections: SRX and grain growth kinetics, and DRX kinetics. These topics are included as 2 separate chapters, as individual papers.

In the first half of this project, samples are cold rolled to induce homogeneous internal strain. Samples are heat treated at temperatures of 350°C-400°C at annealing heat treatment times from 6hr-60hr. In order to analyze grain size, texture evolution and physical properties in these alloys, microstructural characterization and hardness testing were performed. This analysis gave insight into how SRX and grain growth kinetics are affected by variations in precipitate and solute volume fractions.

In the second half of this project, small cylindrical compression specimens are compression tested on the Gleeble 3500 thermal-mechanical simulator to simulate different conditions that initiate DRX. Each alloy is tested at various strain rates and temperatures. Microstructrual characterization and calculations of activation energy (Q) determine specifications of DRX initiation and texture evolution as a function of precipitate and solute volume fraction within these Mg-Zn-Ce alloys.

1.1 Thesis Outline

The outline for this thesis is as follows:

- Background and literature review specific to the experiments performed during this project
- SRX and grain growth experimentation, analysis and results
- DRX experimentation, analysis and results
- Conclusions and future work

1.2 Research Statement and Objectives

The problem this research focuses on addressing is that current literature on recrystallization and grain growth only focus on texture modification and grain size reductions, and are not industrially viable. The objective of this project is to study and analyze the effects of varying precipitate and solute contents on recrystallization and grain growth kinetics. This research determines the effects of these kinetics on hot working parameters and material properties of variations of Mg-Zn-Ce alloys.

Three primary questions led the investigation during this project.

- 1. What is the effect of varying solute and precipitate content on recrystallization and grain growth kinetics?
- 2. What are the microstructural and physical properties affected by enhanced or retarded recrystallization and grain growth kinetics?
- 3. How do lab-scale recrystallization and grain growth processing conditions translate to optimized industry processing parameters for Mg-Zn-Ce alloys?

CHAPTER 2
BACKGROUND AND LITERATURE REVIEW

This chapter focuses on the recent exploration of Magnesium(Mg) alloys within the research community and all background associated with the current project.

2.1 Wrought Mg Alloys

Mg has a hexagonal close packed (HCP) structure and has limited ductility, due to a limited number of independent slip systems. Mg wrought alloys have many useful applications, but their properties are hampered by poor ductility and formability, especially at room temperature. Common extrusion alloys are ZK61 (Mg-6wt%Al-1wt%Zn) and ZK60 (Mg-6wt%Zn-0.6wt%Zr), while common forging alloys are ZK80 (Mg-8wt%Al-0.5wt%Zn) and also ZK60 (Mg-6wt%Zn-0.6wt%Zr)[1]. These prominent lightweight alloys are commonly used in the transportation industry, automotive industry, and aircraft industry. Some of the challenges to using Mg alloys for various applications are the cost and overall alloy properties which include poor formability, anisotropy, low tensile strength at high extrusion speeds and low ductility at high strengths. The basis of much Mg wrought alloy development is combating strong fiber and basal texture of rolled Mg alloys [1]. Doing this involves activating non-basal slip, as well as promoting recrystallization mechanisms to cause texture randomization. Both particle-stimulated nucleation (PSN) and twin-induced nucleation (TIN) are methods that lead to recrystallization of new grains. PSN drastically refines grains in Mg alloys and in turn increases both yield and tensile strengths. Non-basal slip can also be activated through changes in the lattice parameters of Mg, even at moderate temperatures [1]. These processes lend ways towards better processing and properties of wrought Mg alloys.

2.1.1 ZK60 and Modified ZK60

ZK60 has a nominal composition of Mg, 5.8 wt% Zn, and 0.65 wt% Zr. ZK60 is ideally suited for this study because it is a commercial alloy with insoluble Mg-Zr precipitates that influence both grain size and recrystallization. This is an extrusion alloy that experiences precipitation hardening and exhibits a finer microstructure after solidification, hot work, or annealing processes, because precipitates inhibit grain growth [2]. ZK60 is commonly used in aircraft applications, such as landing gear, and modes of transportation, due to light weighting properties. Rare earth elements, such as cerium(Ce) and lanthanum(La), can be added to improve both high temperature strength and creep resistance in ZK60. Compared to other alloys, such as Mg-6.2wt% Zn (Z6) alloys, ZK60 exhibits a finer microstructure after

melting, solidification, or cooling processes, as Mg-Zn-Zr precipitates inhibit grain growth [2]. Ce substitutions, up to 0.4 wt%, can dramatically change the microstructure and tensile properties of ZK60, due to the development of new Mg-Zn-Ce precipitates. X-ray diffraction (XRD) of a Ce-containing (3 wt%) demonstrated that, in addition to Mg_7Zn_3 that exists in base ZK60, a new precipitate $MgZn_2Ce$ forms in the presence of Ce [3]. Applying the extrusion process on cast Mg alloys significantly refines the size of both grains and precipitates. DRX further causes grain refinement in these alloys. The increase in precipitates caused by Ce additions can enhance both hardness and strength of a ZK60 alloy, while minimally influencing elongation.

Nominal ZK60 composition follows ASTM B91-17 [4]. These compositions are varied into three categories: low solute, medium solute, and high solute content. For each of these categories, the compositions are further varied into complete solid solution, 1% pinning phases, or 3% pinning phases. These controlled variations in composition allow for statistical comparison to deem the significance of Ce additions into Mg-Zn-Ce alloys, and can further be elucidated to the addition of rare earth (RE) elements into Mg alloys.

2.1.2 Principles of Extrusion

Over the past decade, research has further focused on processing Mg alloys as wrought products, such as by extrusion. The standard for extrusion of Mg alloys in industry is ASTM B107/B107M-13. This standard is a general guideline for extrusion of Mg alloys in the form of bars, rods, profiles, tubes, and wires [5]. Mechanical requirements depend on geometry and cross-section of the extrudates. This standard also includes dimensional tolerances for each extrudate, including straightness, length, angles, roughness, radius and flatness. The experimental ZK60 material used for this project conforms to this standard. The alloys evaluated in this study are previously extruded via direct extrusion.

In direct extrusion, or forward extrusion, a billet inside a container is forced by a ram through a die opening. This also means that the direction flow of metal is parallel to the ram. Benefits of direct extrusion include continuous extrusion, lower cost than other extrusion options, extrusion of longer extrudates, and production of complex shapes. Yet, there are certain disadvantages to consider when directly extruding, which can impact microstructure and properties of Mg alloys. Contact between the billet and the container results in surface friction and can cause surface cracking. Another major disadvantage of direct extrusion is heterogeneous metal flow and resulting localized heating. This can cause surface tearing and unequal recrystallization kinetics. It is common for recrystallization to occur more quickly at the surface than towards the center, yet this localized recrystallization or grain growth can depend on die speed and reduction ratio [6]. The orientation of each sample with respect to extrusion

direction and rolling direction is included as Figure 2.1.

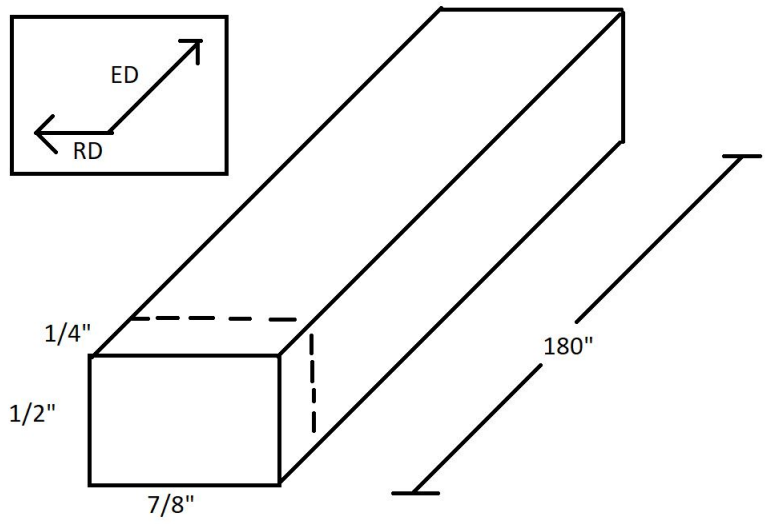

Figure 2.1 Sample orientation with respect to extrusion and rolling directions. The surface analyzed through microstructural characterization is the front facing surface.

2.2 Elemental Analysis

The forefront of Mg research is to improve both formability and strength. Alloy design is essential to both improve formability, while maintaining sufficient strength requirements for specified applications. An essential step in developing alloy design is understanding how composition affects microstructure and properties. Specific alloy additions, such as RE elements, can induce precipitation and control texture through deformation and thermal processing [7]. Other additions in Mg alloys, such as Zn, can cause various amounts of solute distribution throughout the Mg-matrix and cause solute drag. Analysis of elements within the microstructure can identify how texture, microstructural features and processing affect mechanical properties. For example, poor formability can result from development of strong basal texture during rolling, heat treatments or deformation. Addition of RE elements to Mg alloys can allow for increased non-basal texture during SRX/DRX that can in turn increase ductility due to varied deformation mechanisms.

2.2.1 Analysis Methods

There are multiple ways to analyze elemental distribution and chemical composition of materials in a lab setting. The methods utilized in this research are: energy dispersive x-ray spectroscopy (EDS) and x-ray diffraction (XRD) via phase analysis.

Chemical analysis of a certain sample volume can be collected through EDS. EDS can allow for capturing features and phases as small as 1 µm. EDS on the scanning electron microscope is a process of detecting x-rays emitted off the sample, while being bombarded by an electron beam to characterize composition. Electrons are ejected from the atomic shell and the vacancies are filled by higher state electrons. X-rays with energies characteristic of specific elements are emitted to compensate for the electron energy difference. The detector measures the abundance of emitted x-rays versus energy. The information received is presented as an EDS spectrum displaying x-ray energy versus counts. Another analysis technique is XRD, which can be used to develop diffraction patterns and identify phases. This technique provides information on how the structure may deviate due to solute effects, defects, or internal strain distribution. During a scan, x-rays interact with electrons of atoms and scatter. An array of electrons create waves that either, through destructive interference cancel out, or add constructively. Electromagnetic waves impinge on the array of electrons and develop x-ray diffraction patterns. This non-destructive analysis technique can determine atomic arrangement and crystalline orientation.

2.2.2 Solutes and Precipitates

The placement, amount, and composition of precipitates and solutes is responsible for many advantageous properties within Mg alloys. Small impurity regions form in a material when they are no longer able to dissolve into the matrix, formally known as precipitates. Solutes are the result of simply dissolving one metal into the matrix metal, i.e. dissolution of Zn into the Mg-matrix. EDS is the technique used to understand the approximate composition and placement of Mg-Zn-Ce precipitates in this work.

2.3 Recrystallization Fundamentals

Recrystallization is a pervasive transformation phenomenon that is essential in designing material microstructures [8]. Structural factors exclusive to Mg alloys influence both the driving force and recrystallization behavior yielding outcomes distinct from traditional alloys. Deformation processes and material factors, such as stress accumulation, strain distribution, available slip systems, and grain size, can determine details of recrystallization mechanisms and kinetics in the Mg-Zn-Ce alloys studied in this work.

Recrystallization refers to the group of processes that cause stress relaxation in various levels in a deformed metal by releasing stored energy generated from deformation processes post-heat treatment at appropriate temperatures [9]. Recrystallization nucleation mechanisms were first mentioned in 1885 [9], then in works of Cahn [10], Cottrell [11], and various other works throughout the years. Main breakthroughs in recrystallization studies involved understanding recrystallization mechanisms in steps, by breaking down metallurgical reactions such as solid solution decomposition and phase coalescence.

Although under contention for years, it was decided that the nuclei that give rise to new recrystallized grains are already present in the deformed state, where high local orientation gradients constitute the pre-deformed nuclei [12]. The driving force for recrystallization is either thermal or strain energy. This driving force can also be stated as the stored energy that causes competition of recrystallization mechanisms and other phase reactions [13]. In Mg alloys the progressive lattice rotation at grain boundaries provides a location for recrystallization to occur.

Workability of Mg alloys at room temperature, due to their HCP crystal structure and low stacking fault energy, is a hinderance to wide-spread utilization of the alloys. Recrystallization processes allow for microstructural changes during thermomechanical processing. Further mechanistic understanding during recrystallization and grain growth allow for tailoring thermomechanical processing parameters to achieve desired engineering properties.

2.4 Static Recrystallization (SRX)

Solute and precipitate content can greatly affect SRX kinetics. Recrystallization is a process where new stress-free grains nucleate and grow around an original set of grains until full consumption. SRX refers to when recrystallization takes place after plastic deformation (i.e. cold rolling) and subsequent heat treatment. Quantifying and characterizing the effect of varying solute and precipitate content can better enable industrial processing pathways. Zener pinning and solute drag effect both readily impede the rate of SRX and can improve thermomechanical properties of Mg alloys.

2.4.1 Fundamentals

Quantifying and understanding SRX is essential in developing processing parameters for Mg alloys. Microstructure and texture evolve during recovery and SRX, because grains refine and homogenize the distribution of second phase particles. Mg alloys commonly exhibit formability limitations at room temperature, due to their hexagonal close packed (HCP) crystal structure. HCP materials lack the five independent slip systems required for homogenous plasticity. With thermomechanical processing, such as SRX, non-basal slip systems, such as pyramidal and prismatic slip, activate at elevated temperatures increasing formability. Understanding SRX processes is essential to develop high performance Mg alloys.

Precipitation strengthening is a prevalent strengthening mechanism of Mg alloys containing rare earth elements [14]. Ce additions specifically are known to improve the yield strength of ZK60 alloys due to Mg-Zn-Ce particles, and grain growth can be additionally pinned by these particles [15]. Cerium additions are known to reduce grain size of as-extruded ZK60 alloys and grain refinement continues after thermomechanical processing. Solute drag-effect also readily impedes SRX, due to presence of solutes. In

ZK60 alloys, Zn is both a solute within the Mg-matrix and a component in Mg-Zn-Ce precipitates. Understanding recrystallization kinetics of Mg alloys with solutes and precipitates allows for both the control and prediction of microstructure morphology after production processes. Zn is a main element in ZK60 alloys, as well as various other alloys. Zn solutes segregate towards grain boundaries during recrystallization and reduce grain boundary mobility. Fine Mg-Zn-RE and Mg-RE precipitates also act as a retarding force in ZK60 alloys during SRX, and can be utilized to balance both retained strength and ductility. In addition to RE additions notably enhancing the strength and creep resistance of Mg alloys, RE additions in ZK60 alloys are also known to increase stacking fault energy (SFE) [16]. During deformation and annealing required for SRX, SFE has a significant impact on microstructural evolution. When SFE is higher, cross slip occurs more easily because extended dislocation width is small. After Ce addition in Mg-Zn-Ce alloys, precipitates preferentially segregate towards stacking faults and increase stacking fault energy, while promoting activation of non-basal slip. Alloying Mg-Zn alloys with RE elements may cause weaker textures during deformation processing and subsequent annealing [2]. Zener drag contributes to this phenomenon, and analysis of grain sizes and corresponding volume of second phase particles can further explain this phenomenon. Increased amounts of second phase particles increase grain boundary impediment and further stabilize grain sizes during SRX. Zener pinning theory only takes into consideration interfacial energy when quantifying pinning [17]. This theory describes the influence of particle dispersions on grain boundary movement. The relationship of composition, quantified SRX, and texture is the primary basis of the SRX/grain growth part of this study.

2.5 Grain Growth Fundamentals

Grain growth is the subsequent process to SRX where statically recrystallized grains grow. SRX and grain growth are a function of temperature and texture evolution varies for each process. Although RE-texture and non-basal oriented grains can cause advantageous properties during SRX and DRX, grain growth can cause basal texture strengthening and decreased ultimate and yield strengths [18]. The Zener pinning effect of Zn solutes and precipitate pinning of Mg-Zn-Ce precipitates impede grain growth. Increases in pinning decrease grain boundary migration and increase the activation energy (Q) required for grain boundary migration. Determining the specific Q of grain growth, associated texture development and mechanical properties lends insights into industry processing effects on Mg-Zn-RE alloys for engineering applications.

2.5.1 Grain Growth Modeling

Grain growth modeling develops an understanding of how temperature, composition and processing conditions impact grain growth kinetics of a specified alloy under static conditions. Grain growth models of recrystallized grains are understudied for Mg alloys and can give insights into how annealing times can affect material properties. The grain growth model proposed by Robert is utilized to describe the kinetic processes of grain growth in these alloys [19]. Further description of the utilized modeling equations are included in chapter 3. The process of grain growth of recrystallized grains is due to grain boundary migration. A major factor that inhibits the kinetics of grain growth is hard, secondary stable phases that cause grain boundary pinning. Rare earth elements that have low diffusion constants, like Ce, can also inhibit grain growth. Further understanding of strengthening mechanisms can be given by the Hall-Petch coefficient. The Hall-Petch coefficient for Mg is approximately 4.1 times larger than that of aluminum(Al) [19]. The grain strengthening effect within Mg alloys is much greater than comparable light weighting alloys, such as common Al alloys. Both increases in precipitate and solute content can potentially impede grain growth rates, yet to what extent must be evaluated.

2.5.2 Hardness and Physical Properties

Hardness testing at each subsequent annealing step can give insights into how mechanical properties differ and how they are affected by each processing condition. Although SRX causes grain coarsening, softening occurs to a small extent throughout the process. The presence of hard particles due to RE elements can cause increased ductility, while maintaining strength. Grain growth further increases grain size and decreases hardness. Ductility increases during grain growth, but with large decreases in strength that can be unsuitable for a given material application. Although this project focuses on annealing times up to 60h that might not necessarily occur in industry processing, this data displays exactly to what extent grain size, texture and properties change.

2.5.3 Texture Evolution

Texture evolution significantly varies, depending on composition and processing conditions throughout both SRX and grain growth. Mg-rare earth (RE) alloys are known to exhibit texture weakening during deformation processing and subsequent annealing [20]. Zener drag specifically due to the addition of RE elements is the cause of weaker texture. Solutes preferentially segregate towards stacking faults and also increase stacking fault energy, which further activates non-basal slip. Development of non-basal slip that develops during SRX is advantageous for mechanical properties. Subsequent grain growth can cause preferential growth of basal or non-basal grains, and be deleterious to the material properties developed

during SRX. Modeling to what extent texture develops during grain growth gives insight into how specific alloys should be processed in industry.

2.6 Dynamic Recrystallization (DRX)

There is an improved understanding of DRX on the phenomenological level for ZK60, due to research into microstructural changes throughout the DRX process. There is considerable lack of understanding of the underlying physical processes that control DRX. Grain refinement and associated improvement in mechanical properties during thermomechanical processing are commonly attributed to dynamic recrystallization (DRX), due to low stacking fault energies (SFE) that result. DRX proceeds through nucleation and growth and is commonly the slowest, rate-controlling process for Mg alloys [21]. During hot deformation of materials with low to moderate SFE, the formation of new grains occurs by conventional DRX—i.e., twinning [22], nucleation [23] and subgrain rotation [24]. Recently, newer mechanisms of DRX have been found to operate at lower temperatures [21]. Different mechanisms of DRX are operative in ZK60 Mg alloys at different deformation temperatures. DRX mechanisms are directly related to deformation conditions, and therefore are affected by operating parameters of deformation processes. Despite this information, not enough quantitative data has been published to elucidate an interdependence of deformation and specific DRX mechanisms in ZK60 Mg alloys, especially without varying Mg(Zn,Zr) precipitate fractions.

2.6.1 Fundamentals

DRX is recrystallization that occurs after plastic slip is introduced and energy accumulates throughout the structure. When plastic deformation occurs, DRX reduces the stored energy. Continuous DRX (CDRX) is the dominant mechanism of DRX in Mg-RE alloys. CDRX occurs at rotated lattice regions near grain boundaries through subgrain rotation during compression within the deformation temperatures of this study [25]. Particle stimulated nucleation (PSN) also occurs in the regions of secondary phase particles, and is a main cause of texture weakening. Other causes of texture weakening in Mg alloys include particle pinning, solute drag and ease of shear band formation [26]. All of these phenomena are common in Mg-RE alloys and for this reason RE elements, such as Ce, advantageously increase strength and ductility after processing. Modeling of DRX processes in Mg-RE alloys is essential to give insight into ideal processing conditions under deformation temperatures and strains.

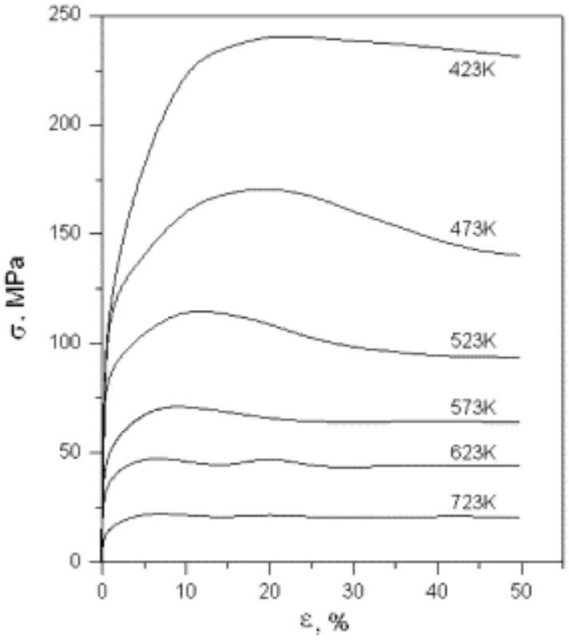

Figure 2.2 Flow curves for a nominal ZK60 alloy processed at a strain rate of $2.8 \times 10^{-3} s^{-1}$ [21]. Copyright approval for this figure is included in the Appendix.

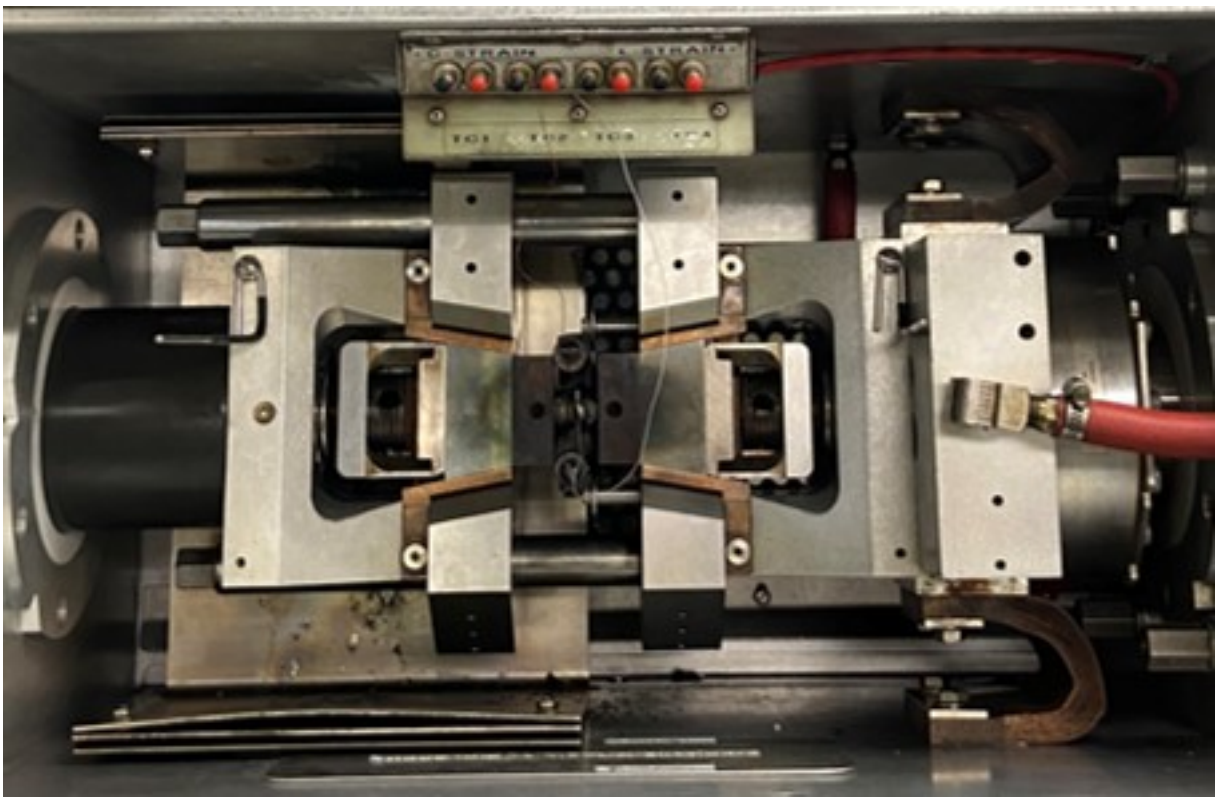

Figure 2.3 Gleeble 3500 thermomechanical simulator with a sample after compression testing.

2.6.2 Modeling and Flow Curves

Flow curves can give insight into DRX for Mg alloys. It is characteristic for flow stress to increase to a maximum, and then decrease to a steady state under circumstances of hot working accompanied by DRX [21]. Per prior approval, a schematic displaying flow curves for a standard ZK60 Mg alloy compression tested at a strain rate of $2.8x10^{-3}$ s^{-1} is included as Figure 2.2. At low temperatures, the flow curve exhibits high peak stress and high peak strain, then minimal work softening after the peak. At moderate temperatures the flow curves exhibit more work softening after the peak. At the highest temperatures, steady state is attained after small peak stress and strain, with very minimal work softening. These correlations lead to further evaluation of peak stress and activation parameters required for DRX.

Thermomechanical testing of Mg alloys are commonly completed on a Gleeble. Figure 2.3 is an example of a Gleeble with a cylindrical sample between the 2 anvils, specifically the Gleeble 3500 thermomechanical simulator. This is the machine used for DRX simulation in this study. A sample after compression testing, with thermocouples attached, and after testing are included as Figure 2.4.

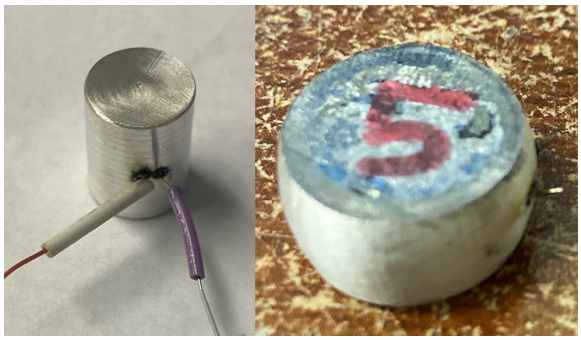

Figure 2.4 Gleeble samples before and after a compression test completed to 0.8 true strain. The dimensions of the sample before testing are d(10mm)xh(15mm).

2.6.3 Activation Energy

The activation energy, Q, for DRX can be calculated to determine how much energy input is required for the initiation of DRX. Composition and previous processing cause variations in the required Q for DRX. In Mg-Zn-RE alloys, presence of an RE element and increases in Zn can cause the required Q to increase due to solute drag effect and precipitate pinning. The value of Q can be calculated through variations in stress and critical stress curves and DRX modeling. Q can also be determined by equations for the Zener-Hollomon parameter [27], which is determined based on strain rate, Q, temperature and other constants. Determining Q is just one step in building constitutive equations for each alloy under standard strain rates and temperatures and assists in making informed processing decisions.

CHAPTER 3

EXPERIMENTAL METHODS

This chapter includes details of experimental methods, additional trials and experiments that were conducted and not included in the papers within this thesis, as well as supporting information.

3.1 Experimental Material

The experimental material was initially received in extruded billets, as shown in Figure 3.1. Before being received the material was gravity cast in steel molds and homogenized at 400°C for 24 h. They were then extruded at 388°C with a die exit speed of 2.5-3.3 ft/min, reduced at a ratio of ~19.0 and air cooled to room temperature.

Figure 3.1 Received experimental material in billet form

These billets have a cross-section geometry of 1/2”x7/8”. The alloy compositions are included as Table 3.1. There are 2 billets for each alloy, totaling 5 alloys. Samples for SRX and grain growth trials were cut transverse to the extrusion direction to a 1/4” thickness. Each sample was pre-strained to 15% reduction in thickness before static annealing via cold rolling. This amount was determined through preliminary cold rolling trials.

Table 3.1 Compositional matrix (all in wt.%) for five alloys studied, varied by volume fraction and percent pinning phases.

	Complete solid solution	~1% pinning phases	~3% pinning phases
Low solute	~	LZ-0.4Ce (Mg-1.40Zn-0.38Ce)	~
Med solute	~	MZ-0.4Ce (Mg-3.52Zn-0.38Ce)	~
High solute	HZ-0Ce (Mg-4.21Zn)	HZ-0.1Ce (Mg-5.26Zn-0.12Ce)	HZ-0.3Ce (Mg-6.78Zn-0.31Ce)

3.2 Material Preparation

The sample preparation required before microstructural characterization via EBSD and hardness testing is outlined in Table 3.2.

Table 3.2 Detailed polishing procedure of experimental Mg-Zn-Ce samples.

Step	Details	Time
Grinding	200, 400, 600, 800, 1200 grit	N/A
Polishing	6µm, 3µm, 1µm	∼3min/step
Polishing	0.05µm	∼1.5min
Sonicate	isopropanol	∼20 min

The polishing procedure starts with sectioning samples with a high-speed abrasive wheel and mounting them in cold epoxy. The cold mount epoxy used had a maximum curing temperature of 40°C. Samples were left to cure for 24 h before grinding. Samples were then ground to 1200 grit. Between each grinding step, samples were cleaned with water and soap. Samples were then polished from 6µm to 1µm for ∼3 min with water-free diamond solution on low nap pads. The last polishing step was at 0.05µm with a high nap pad. Between each polishing step, the surface was etched in a picric-acetic acid solution: 3g picric acid, 10mL acetic acid, 10mL DI water, 70mL ethanol. Also between each polishing step samples were cleaned with isopropanol. Optical microscopy was conducted to ensure adequate polishing. Before microstructural characterization, samples were sonicated in isopropanol for ∼20 min. Only after these steps were completed were samples analyzed via EBSD.

3.3 Preliminary Cold Rolling Trials

Pre-straining is necessary to understand the effects of deformation on SRX and grain growth kinetics. Cold rolling is a consistent method for pre-straining and approximately 20-30% deformation is needed for effectiveness [53]. Cold rolling increases hardness uniformly, due to an increase in stored strain energy. For this trial, sections of each of the 10 extrudates were machined to the geometry of 1/2" x 7/8" x 1/4". Each section was rolled longitudinal to the extrusion direction, with the goal to determine the maximum reduction in thickness possible. The exact geometry of each specimen and achieved percent reductions in thickness are included in Table 3.3.

The goal of these preliminary trials was to determine the amount of cold work necessary before static heat treatments to allow for maximum SRX at each time and temperature combination. It was also important to determine the maximum strain per pass that was repeatable within all of the SRX and grain growth samples. These trials determined that it was only realistic to get about 15-20% reduction in thickness and that above ∼2.5% strain per pass there are greater quality issues, such as cracking. These results were used to determine the 15% reduction in thickness was sufficient before static annealing in the SRX and grain growth trials within this project. It is possible that small increases in strain past 15% could speed up SRX and grain growth rates. Further cold rolling trials would need to be conducted in the future to confirm this.

Table 3.3 Cold rolling trials to determine the optimal rolling procedure conducted in Chapter 4. Reduction is measured as reduction in thickness.

Alloy	T_i(in)	T_f(in)	Passes	Reduction(%)	True Strain/pass(%)
LZ-0.4Ce	0.338	0.296	11	12	1.09
LZ-0.4Ce	0.321	0.281	11	12	1.13
MZ-0.4Ce	0.324	0.275	12	15	1.26
MZ-0.4Ce	0.351	0.316	8	10	1.24
HZ-0Ce	0.365	0.275	8	25	3.08
HZ-0Ce	0.348	0.274	9	21	2.36
HZ-0.1Ce	0.286	0.233	8	19	2.32
HZ-0.1Ce	0.347	0.291	9	16	1.79
HZ-0.3Ce	0.251	0.201	8	20	2.49
HZ-0.3Ce	0.249	0.205	8	18	2.21

3.4 Microstructural Characterization via EBSD and Grain Size Analysis

In the SRX and grain growth section of this project, EBSD was performed on all alloys and processing conditions. The analyzed surface was longitudinal to the rolling direction and transverse to the extrusion direction. In the DRX section of this project, EBSD was conducted on each sample after compression testing at specified strain rates and temperatures. The analyzed surface of the compressed samples is longitudinal to the compression and extrusion direction, and transverse to the rolling direction. The characterized surface was polished to 0.05µm, sonicated in isopropanol and EBSD was performed within 1 hour of polishing. EBSD mapping analysis was performed with a 20kV electorn beam, 18mm working distance and 2µm step size. 5 inverse pole figure (IPF) maps were taken in multiple areas of each sample surface and processed with Neighbor Pattern Averaging Indexing (NPAR) in Orientation Imaging Microscopy (OIM). NPAR is responsible for averaging neighboring grain patterns and improving the signal to noise ratio. OIM provides a automated method for determining the grain sizes of each grain in the microstructure. Average grain sizes for each alloy and processing condition was determined for each of the 5 IPF maps, then averaged. The total area surveyed for each sample was 2000 x 2000µm. This data was utilized to develop a grain growth model and conduct preliminary analysis of texture.

3.5 Texture Analysis

Qualitative preliminary texture analysis was conducted utilizing the IPF maps obtained for each sample. Referencing the orientation key, grains were categorized as near-basal or non-basal. This initial observance identifies texture weakening effects that occur during SRX and preferential growth of basal grains during grain growth. This analysis sets the basis for in-depth analysis of texture in future studies.

3.6 Hardness Testing

The AMH55 Hardness Testing System was utilized to conduct Vickers microhardness (HV) testing on each as-received, as-cold rolled and statically annealed sample within the SRX and grain growth section of this project. 20 automated linear hardness intents were done on each sample surface with a 300g load and 10s hold time, then averaged. These hardness tests were performed on the same surface that was imaged with EBSD, the surface transverse to the extrusion direction and longitudinal to the rolling direction. These values were then used to compare to grain size and texture at each annealing time frame. These values were evaluated at each step within the SRX and grain growth kinetic processes that were evaluated during this project duration, and is included in Chapter 4.

CHAPTER 4

SOLUTE AND PRECIPITATE EFFECTS ON STATIC RECRYSTALLIZATION AND GRAIN GROWTH KINETICS OF CE-CONTAINING MG ALLOYS

A paper to be submitted to *The Journal of Metallurgical and Materials Transactions A*

Storey, G.K.[1,2]; Sutton, S.[3,4]; McBride, B.N.L[1,5]; Hartman, D.[3,4]; Clarke, A.J.[1,4]; Clarke, K.D.[1,4]

4.1 Abstract

Static recrystallization (SRX) and grain growth kinetics of Mg alloys can vary greatly based upon precipitate and solute contents. Rare earth alloying elements, such as Ce, have been shown to stabilize grain size at elevated temperatures and thereby improve elevated-temperature properties. Quantifying the effects of precipitate fraction and solute content can result in fundamental understanding to enable optimized industrial processing pathways. The baseline composition for this study is ZK60. Several variations on ZK60 compositions with different Zn and Ce levels were evaluated, which result in variations in second phase insoluble particle type, solute distribution, and volume fraction that have strong effects on both grain size and recrystallization. Aspects of quantitative determinations of precipitate and solute contents as a function of alloying are related to recrystallization kinetics. These results provide further insights into mechanical and microstructural characteristics, including hardness, grain size distribution and texture, which are affected by enhanced or retarded recrystallization and grain growth kinetics. The results show that increases in precipitate and solute contents due to increasing Zn and Ce contents increase Zener pinning and solute drag and decrease grain growth kinetics. Texture weakening is observed to occur during SRX, and basal grains grow preferentially during grain growth. Evaluation of grain growth gives insights into how variations in temperature and static annealing time affect microstructure and associated texture development.

4.2 Introduction

Wrought Mg alloys are valuable for lightweight structural applications, due to a high strength-to-weight ratio [28]. Deformation is limited at room temperature, because of a lack of the five independent slip systems required for homogenous plasticity. Thermo-mechanical processing, such as elevated temperature extrusion, allows for non-basal pyramidal and prismatic slip systems to be active during deformation.

[1]Center for Advanced Non-Ferrous Structural Alloys (CANFSA), Metallurgical and Materials Engineering Department, Colorado School of Mines, Golden, CO 80401, canfsa.org
[2]Primary researcher and author
[3]Mag Specialties Inc., Denver, CO, 80210
[4]Mentorship and guidance
[5]Assistant to research and theory

Texture and microstructural evolution changes during recovery and static recrystallization (SRX) can further refine grains and homogenize the distribution of second phase particles. Subsequent grain growth can be detrimental to material properties of magnesium-rare earth (RE) alloys, due to increased grain sizes and texture evolution. Characterizing and understanding microstructural evolution through SRX and subsequent grain growth is thus essential to enable the production of high performance alloys.

The initiation of SRX and associated nucleation and subsequent grain growth are analyzed through microstructural characterization and hardness testing. The improvement of ductility is the focus of recrystallization processes in magnesium-RE alloys. Mg-RE alloys deform by two deformation mechanisms, slip and twinning [29]. Twining accommodates deformation along the c-axis, meaning that larger grain sizes increase the quantity of twinning, while finer grains reduce twinning and increase ductility [30]. Due to the nature of deformation via twinning, excess twinning can significantly decrease ductility. The grain boundaries, twins and shear bands can be preferential sites for nucleation of recrystallized grains, as determined by characterization. The majority of these initially nucleated grains are non-basally oriented, and this orientation is commonly referred to as the RE-texture orientation [29]. The specific nucleation sites for Mg-RE alloys are determined by the dominant deformation mechanisms. The deformation mechanisms present in these alloys are thus controlled and observed by texture differences.

Precipitation is a primary strengthening mechanism in Mg alloys containing RE elements [14]. In ZK60 alloys, Zn is a primary alloying element and is both a solute within the Mg-matrix and a component in Mg-Zn-Ce precipitates. Understanding recrystallization and grain growth kinetics of alloys with given solute and precipitate contents allows both the control and prediction of the microstructural morphology after production processes. Zn solute segregates to grain boundaries during recrystallization and reduces grain boundary mobility. Fine Mg-Zn-RE and Mg-RE precipitates also act to slow SRX in ZK60 alloys, and can be utilized to tune strength and ductility combinations. The substitution of Ce for Zr at various levels has been shown to improve the yield strength of ZK60 (Mg-Zn-Zr) alloys, due to Mg-Zn-Ce particle strengthening; grain growth kinetics can also be reduced by these particles [31]. Ce additions are known to reduce the grain size of as-extruded ZK60 alloys by inhibiting grain growth, and this grain refinement is maintained throughout thermomechanical processing and subsequent heat treatment. The solute drag-effect also readily impedes SRX, since some Ce is in solution.

In addition to RE additions notably enhancing the strength and creep resistance of Mg alloys [32][33], RE additions in ZK60 alloys are also known to increase stacking fault energies (SFE) [28]. During the prior deformation and annealing required for SRX, SFE has a significant impact on microstructural evolution. When SFE is higher, cross slip occurs more easily because the extended dislocation width is small. In Mg-Zn-Ce alloys, Zn solutes preferentially segregate towards stacking faults and increase stacking fault

energy, promoting activation of non-basal slip and texture weakening. Adding RE elements to ZK60 alloys can result in weaker texture from deformation processing and subsequent annealing [34]. Zener drag contributes to this phenomenon, and analysis of grain sizes and corresponding volumes of second phase particles can provide further insights into microstructural effects on grain motion. Increased volume fractions and number of second phase particles decreases grain boundary mobility and further stabilizes grain sizes and slows SRX and grain growth kinetics. Zener pinning theory only takes into consideration interfacial energy when quantifying pinning [35]. The relationship between composition, initiation of SRX, grain growth kinetics and texture is the primary basis of this study.

4.3 Experimental Procedures

The material used in this study is a modified ZK60 (Mg-Zn-Zr) composition, with deliberate variations in Zn levels and replacement of Ce for Zr in various amounts. The compositional matrix is separated into 3 levels of Zn, varying the hypothesized solute volume, and 3 levels of Ce varying the hypothesized precipitate volume, as shown in Table 4.1.

Table 4.1 Compositional matrix (all in wt.%) for five alloys studied, varied by volume fraction and percent pinning phases.

	Complete solid solution	∼1% pinning phases	∼3% pinning phases
Low solute	~	LZ-0.4Ce (Mg-1.40Zn-0.38Ce)	~
Med solute	~	MZ-0.4Ce (Mg-3.52Zn-0.38Ce)	~
High solute	HZ-0Ce (Mg-4.21Zn)	HZ-0.1Ce (Mg-5.26Zn-0.12Ce)	HZ-0.3Ce (Mg-6.78Zn-0.31Ce)

Zn levels are: low Zn (1.4 wt%), medium Zn (3.5 wt%) and high Zn (4.2-6.8 wt%) and Ce addition levels are: 0% (0 wt%), 1% (0.12-0.38 wt%) and 3% (0.31 wt%) precipitate volume fractions. The volume fractions were the initial composition goals and align the precipitate and solute levels analyzed in this research. The variations in Zn and Ce within these alloys result in changes to second phase insoluble particle volume fractions and distributions. ZK60 is ideally suited for this study, because it is a commercial alloy with insoluble Mg-Zr precipitates that influence grain size and SRX kinetics. This alloy is an extrusion alloy that experiences precipitation hardening and exhibits a finer microstructure after thermomechanical processing. The five alloys were previously gravity cast in steel molds, homogenized at 400°C for 24 h, extruded with a rectangular die with a cross section of 12.7 mm(1/2")x 22. 2mm(7/8") with a die speed of 0.762^{-1} m/min to a reduction ratio of 19.0 and air cooled to room temperature. Mag Specialties Inc. supplied these materials in the as-extruded condition.

4.3.1 Cold Rolling and Heat Treatment

Samples of each alloy were sectioned into the geometry of (12.7mm)1/2"x(22.2mm)7/8"x(6.35mm) 1/4". These samples were cold rolled to 15% reduction in thickness, with 3% strain/pass to increase stored strain energy and provide increased driving force for SRX to occur. The roll size was 3" and each sample was rolled at 48RPM. The rolling direction is transverse to the extrusion direction. Individual samples were then annealed at either 350 or 400°C and held for 6 h, 10 h, 12 h, 18 h, 24 h, 48 h, and 60 h, then oil quenched. Each sample was then mounted, ground, polished to 0.05µm colloidal silica and etched after each polishing step in a solution of 4.2g picric acid, 70 mL ethanol, 10mL glacier acetic acid, and 10mL deionized water, for 10 s [34]. The polished surface for each sample is transverse to the extrusion direction.

4.3.2 Microstructural Characterization

Electron backscatter diffraction (EBSD) was utilized to quantify grain size and texture as SRX initiated and grain growth progressed. EBSD mapping was performed with a 20kV electron beam, 18mm working distance and 2µm step size on the JEOL JSM-7000F Field Emission SEM (FESEM) using the EDAX Hikari Pro 600pps EBSD detector. Each inverse pole figure (IPF) map was processed with Neighbor Pattern Averaging & Reindexing (NPAR) in Orientation Imaging Microscopy (OIM) software. Data was cleaned using neighboring grain orientation correlation in NPAR. The grain size was determined through OIM on 5 IPF maps of each processing condition, then averaged. The total area surveyed for each sample was 2000 x 2000µm. The IPF maps are utilized to determine a grain growth model for each alloy and feature the initiation of SRX in the as rolled and shorter annealing timeframes. Any SRX nucleates observed in the as-received and as-rolled micrographs were not included in grain size measurements, but ranged from 1.7-2.4µm. Fraction of recrystallized grains in the 6 h and 10 h annealed samples is determined by a size threshold where grains with an area <15% than the initially cold-rolled average grain size were deemed to be recrystallized. Grains were also hand counted to account for polygonal grains, equiaxed grains, and absence of internal grain structure to indicate recrystallization.

4.3.3 Hardness Testing

Vickers microhardness (HV) values were determined for each of the annealing stages for as-cold rolled and as-received samples. Hardness values were determined using an AMH55 Hardness Testing System to average 20 linear hardness indents with a 300g load and 10 s hold time, and performed on a transverse cross-section to the extrusion direction. Hardness testing after each annealing step allows for comparison of physical properties, grain size and texture at each annealing time frame.

4.4 Results and Discussion

This section presents all results of experimentation and analysis and discusses the relevance and importance of these results.

4.4.1 Microstructural Characterization

EBSD of the transversely mounted samples for each annealing time at both 350 and 400°C was completed and inverse pole figure (IPF) maps are included as Figures 4.1 and 4.2. The mean grain diameter and maximum grain diameter were determined through OIM and manual methods at each annealing time, and is included as Figure 4.3. The maximum grain diameter is analyzed to determine approximate ranges in mean and maximum grain size at each processing condition. The mean grain diameter decreases during SRX within 6 h for 400°C and within 10 h for 350°C. This is due to faster SRX kinetics at higher temperatures and subsequently finer grain development at shorter annealing times. Alloys with lower Zn contents have a greater decrease in grain sizes during SRX and therefore faster SRX kinetics than higher Zn alloys. The LZ-0.4Ce alloy had a final mean grain size of 31.4 µm +-0.2µm, whereas the HZ-0.3Ce alloy had a final mean grain size of 28.4µm +-0.2µm after SRX at 350°C at 10 h. Ce content had a similar effect, where increases in Ce addition substantially decrease SRX kinetics. The HZ-0Ce alloy had a final grain size after SRX of 34.8µm, much higher than the other high Zn alloys. Ce additions, per wt%, exhibit a greater inhibiting effect on SRX than Zn additions. The trends of composition and SRX kinetics are the same for SRX at 400°C, yet all SRX kinetics are faster.The calculated fraction of recrystallized grains for each alloy at both 6 h and 10 h annealing times are determined and included in Table 4.2.

Texture weakening is observed within samples that undergo SRX. It has been proposed that particle-simulated nucleation (PSN) is the cause for texture weakening effects in Mg-RE alloys [36]. The solid solution alloy (Mg-4.21Zn) also displayed texture weakening effects, so PSN is not a requirement for texture weakening to occur. In Mg-4.21Zn, Zener pinning and solute drag are the contributing mechanisms causing texture weakening. Texture weakening can be difficult to quantify for each processing state, due to recrystallization causing texture to be more randomized in the higher Ce alloys, yet comparing the (0001) inverse pole figures for each processing condition would give insight into the extent of texture weakening during static recrystallization. Texture randomization is important within the SRX process to achieve increased formability and elongation to failure. No correlation between texture weakening and composition is observed in this data, yet is known to be directly related to the rate of SRX. When grain growth starts, basal grains preferentially grow and result in less advantageous material properties. The presence of basal grains can decrease strength and ductility expressed by Mg-Zn-RE alloys in application.

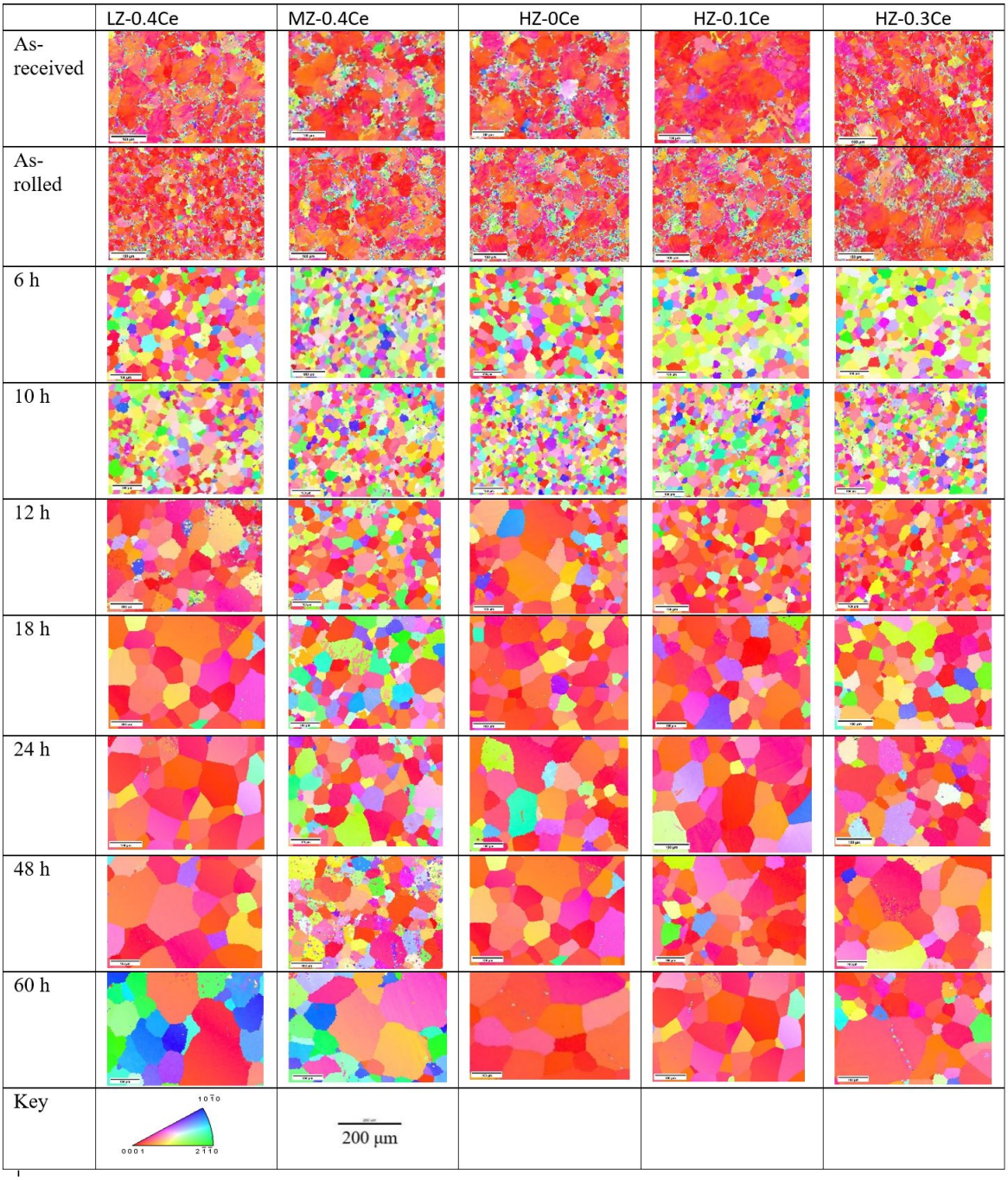

Figure 4.1 Representative IPF maps for as-received, as-rolled, and 350 °C annealed samples. The scale bar for each map is 100 µm and the scan dimensions are 400µm x 400µm. These maps are taken longitudinal to the rolling direction.

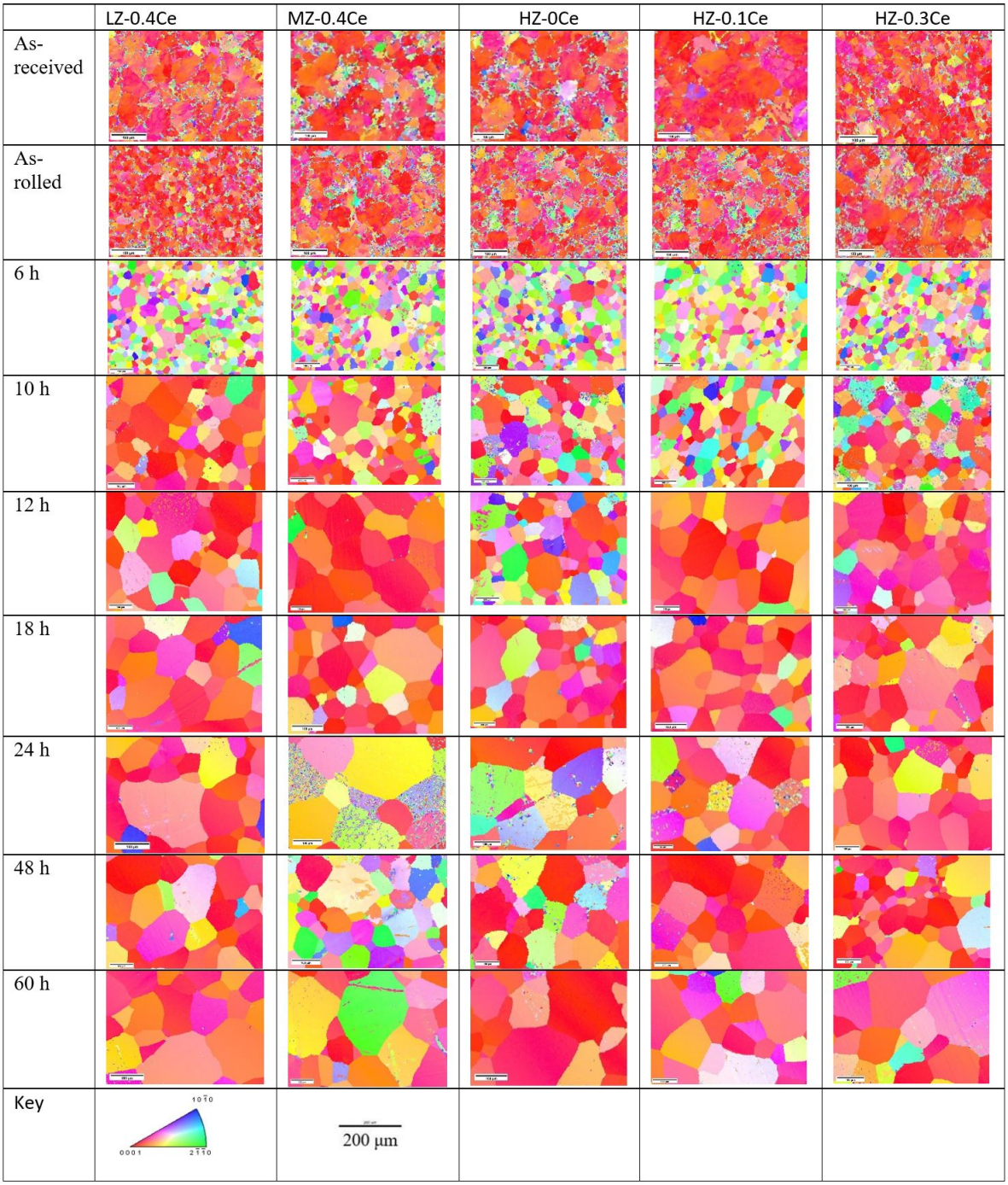

Figure 4.2 Representative IPF maps for as-received, as-rolled, and 400 °C annealed samples. The scale bar for each map is 100 µm and the scan dimensions are 400 µm x 400 µm. These maps are taken longitudinal to the rolling direction.

More annealing times would be required at lower time frames to determine an SRX model for each alloy and SRX is observed in the as-rolled specimens. Non-basal oriented grains have been found to have a higher nucleation propensity at shear bands in Mg-RE alloys [29]. This is observed in the as-rolled condition for

each alloy, where non-basal oriented grains start to nucleate within shear bands and at grain boundaries. The formation of the non-basal RE texture orientation is also known to be suppressed at higher temperatures, especially during extrusion [29], yet would require further quantification in this study to determine to what extent. Further texture throughout SRX can be explained by initial oriented nucleation.

Table 4.2 Determined % SRX values for 6 h and 10 h annealing times for 350 °C and 400 °C for each alloy.

Alloy	6 h(350 °C)	10 h(350 °C)	6 h(400 °C)	10 h(400 °C)
LZ-0.4Ce	58%	88%	91%	100%
MZ-0.4Ce	62%	75%	86%	100%
HZ-0Ce	76%	92%	93%	100%
HZ-0.1Ce	54%	71%	83%	100%
HZ-0.3Ce	45%	68%	82%	100%

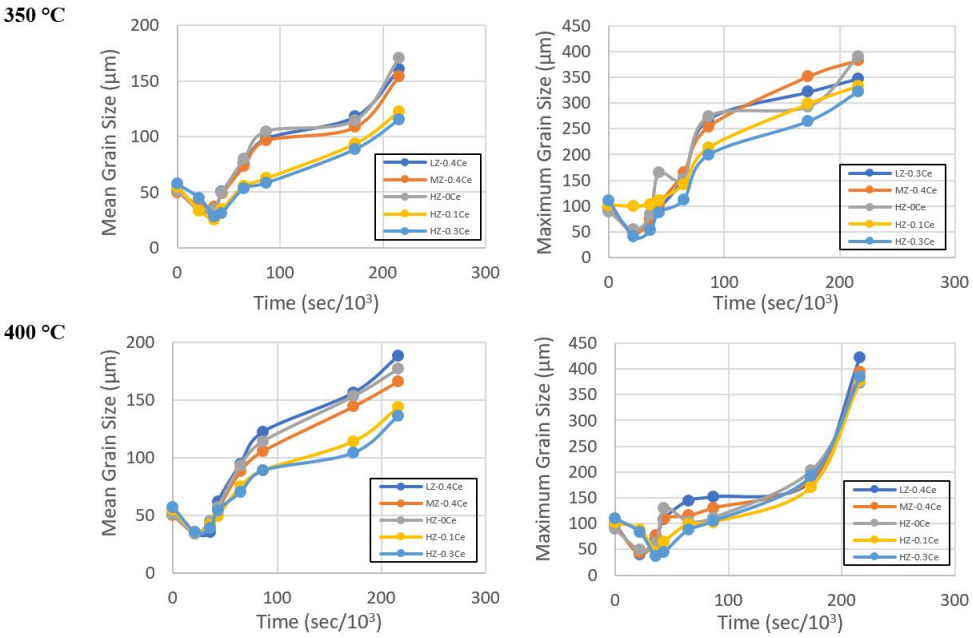

Figure 4.3 Curves of d_{mean}, the mean grain size, and d_{max}, the maximum diameter of recrystallized grains, versus annealing time.

4.4.2 Modeling of Grain Growth

Developing accurate modeling of grain growth processes allows for further grain size and texture control in production annealing processes. Static annealing times of 10 h-60 h at both 350 and 400°C for each of the five alloys are investigated for grain growth. Recrystallization was fully complete for both temperature ranges by 10 h and grains enlarged more quickly at 400°C. Increases in both Zn and Ce has a significant impediment effect on grain growth kinetics. The activation energy for grain growth can be calculated to

elucidate grain growth mechanisms during these static annealing times. Grain growth can be approximated based on the Burke Turnbull equation [19],

$$d^{n'} - d_0^{n'} = kt \tag{4.1}$$

Where d is the grain size at each annealing time, d_0 is the initial grain size at t=0, t is the annealing time and n' is the grain growth exponent, known as 2. k is a constant described by the Arrhenius equation that is temperature-dependent,

$$k = k_o exp(-\frac{Q}{RT}) \tag{4.2}$$

where Q is grain growth activation energy, R is the gas constant and k_o is a constant. The complete equation for D^2 that is utilized for the final grain growth modeling equation is,

$$d^2 = k_o t exp(-\frac{Q}{RT}) + d_o^2 \tag{4.3}$$

Grain size data is further utilized to compare d^2 and t, included as Figure 4.4. The slope of d^2-t is k.

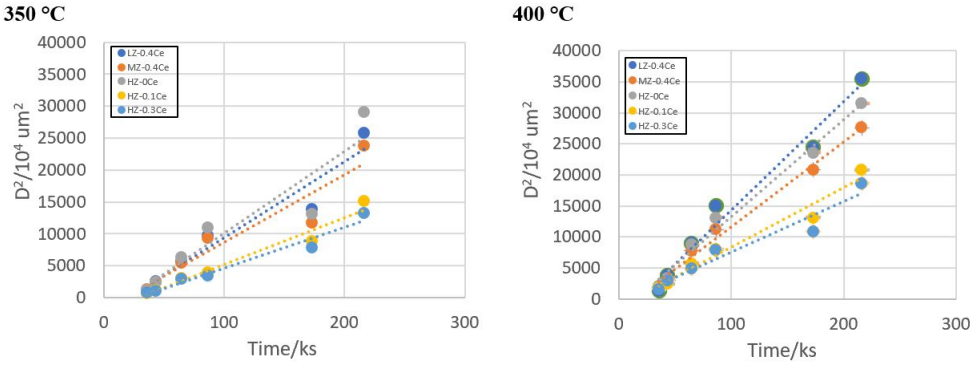

Figure 4.4 Curves of d^2-t with linear fits at 350 °C and 400 °C for each alloy.

The logarithmic form of equation 4.2 is then utilized to compare ln k and 1/T. The linear regression of ln k-1/T gives a slope coefficient of Q/R for each alloy. A graph of these linear regressions is Figure 4.5.

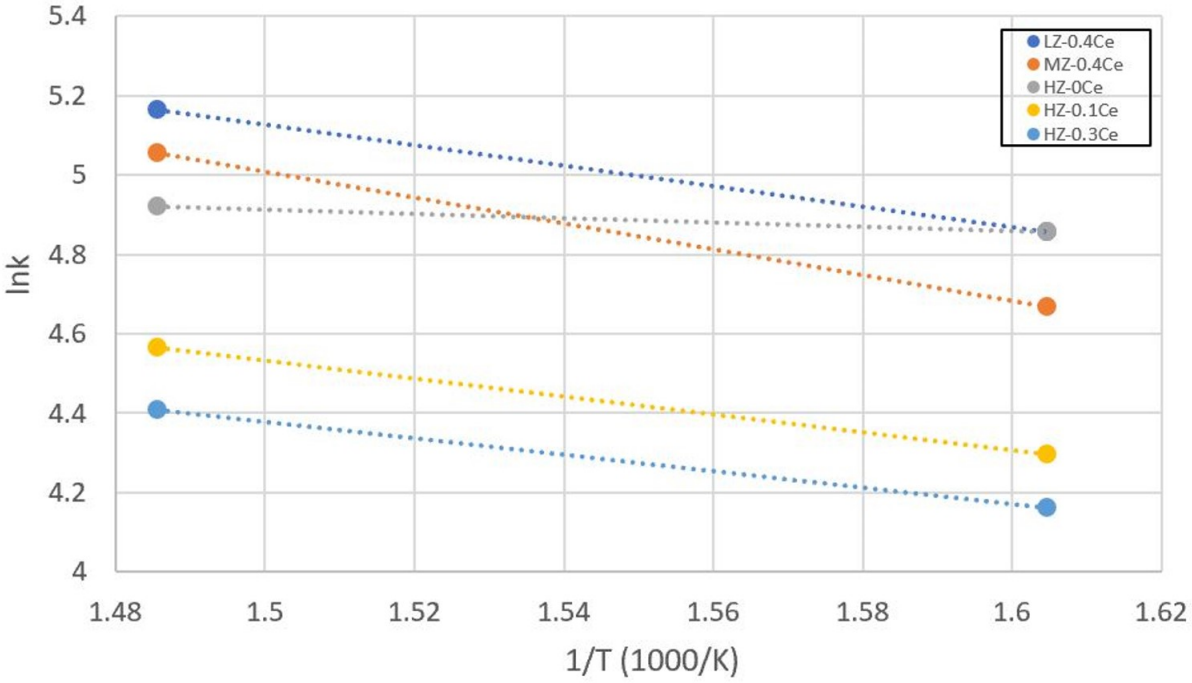

Figure 4.5 Curves of ln k-1/T with linear fits for each alloy.

The calculated values of Q and the final grain growth model analyzed for each alloy, included in Table 4.3, are then compared to observed textures.

Table 4.3 Calculated values of Q and the determined grain growth models for each alloy.

Alloy	Q (kJ/mol)	Grain growth model
LZ-0.4Ce (Mg-1.4Zn-0.38Ce)	44.47	d^2=590176t$exp(-\frac{-5348}{T})$+1125.60
MZ-0.4Ce (Mg-3.42Zn-0.38Ce)	47.89	d^2=957971t$exp(-\frac{-5760}{T})$+1632.16
HZ-0Ce (Mg-4.21Zn)	38.82	d^2=186068t$exp(-\frac{-4669}{T})$+1608.01
HZ-0.1Ce (Mg-5.26Zn-0.12Ce)	52.64	d^2=1533199t$exp(-\frac{-6332}{T})$+1112.22
HZ-0.3Ce (Mg-6.78Zn-0.31Ce)	63.81	d^2=10847275t$exp(-\frac{-7676}{T})$+1142.44

The constant k, based on the Arrhenius equation, is directly proportional to the speed of growth kinetics, whereas speed of growth is inversely proportional to static annealing time, t. From this reasoning, k is inversely proportional to t. The growth activation energy increases for alloys with higher Zn and Ce contents. For the LZ-0.4Ce alloy, the calculated Q value is 30.3% less than the HZ-0.3Ce alloy. For the HZ-0Ce alloy, the calculated Q value is 64.4% less than the HZ-0.3Ce alloy. Increasing the Ce amount dramatically increases the activation energy required for grain growth, due to increases in Mg-Zn-Ce

precipitates and presents a more significant effect than solid solution strengthening alone. The validity of these calculations is determined from literature comparison to grain growth calculations of similar Mg-RE alloys. Xiya et.al. determined Q values of 42.66 and 56.34 kJ/mol for Mg-4.9Zn-0.7Zr and Mg-4.9Zn-0.9Y-0.7Zr [19], respectively. The LZ-0.4Ce alloy in this study has a calculated Q value of 44.47 kJ/mol and varies according to composition variations.

4.4.3 Hardness Testing

Hardness testing was conducted on all annealed samples and gives insight into the softening rates of each alloy through SRX and grain growth at 350 °C and 400 °C. These hardness values are included in a bulleted line graph as Figure 4.6.

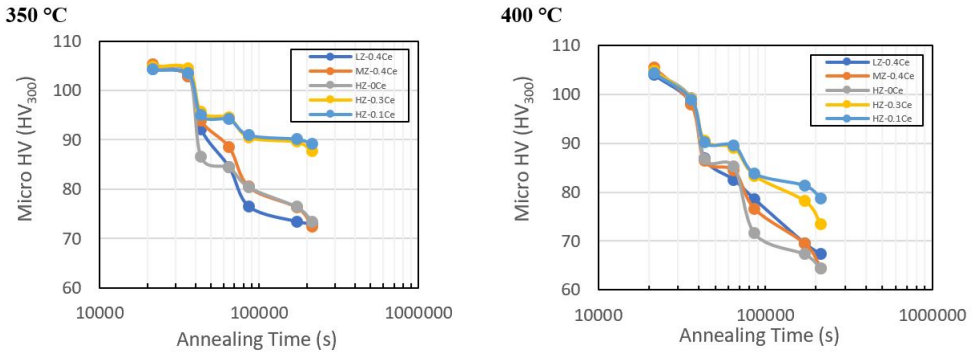

Figure 4.6 Curves of hardness at each annealing time at 350 °C and 400 °C for each alloy.

Softening rates are significantly faster at 400 °C and for alloys with lower Zn levels, with the exception of the HZ-0Ce alloy. The HZ-0Ce alloy has less precipitates causing Zener pinning and precipitate strengthening. When grain growth starts, the softening rate is much more significant than for SRX and is observed to be relatively linear. These hardness values give insight into how mechanical properties are affected by SRX and grain growth kinetics.

4.4.4 Elemental Analysis

Energy dispersive spectroscopy (EDS) results provide an understanding of the distribution and presence of Zn and Ce throughout the Mg-matrix. These results help to understand the correlation between composition, solute distributions, and precipitate distributions. An EDS spectrum was obtained on a deformed specimen of the LZ-0.4Ce alloy to give elemental identification of the bulk sample, which included verification of Mg, Zn, Ce, O (oxides), and Si (colloidal silica). EDS maps of the same alloy display the distribution of Mg, Zn, Ce, and these maps are included within Figure 4.7. Element distribution was further confirmed by EDS line scans, and it is observed that Zn is both in solution in the

matrix and within the precipitates. There is a clear correlation between SRX/grain growth kinetics, Ce concentration and Zn concentration.

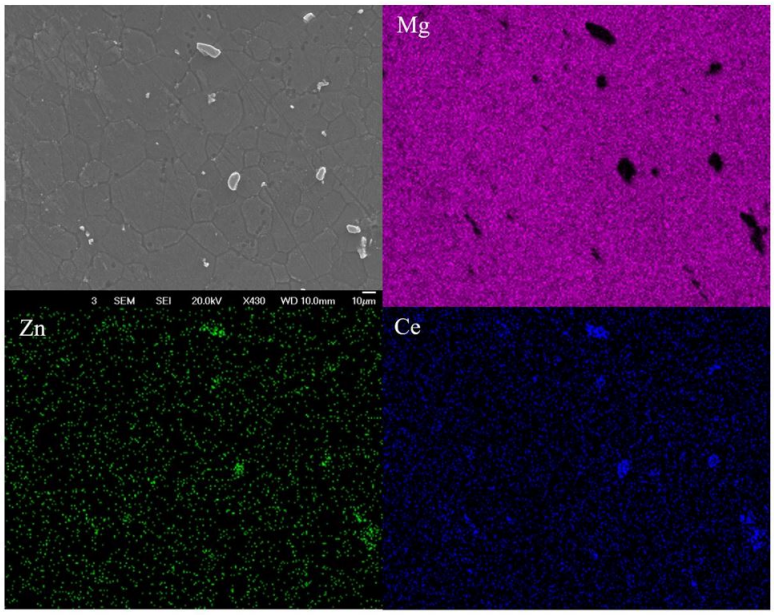

Figure 4.7 EDS maps displaying relative distributions of Mg, Zn, and Ce of as-rolled LZ-0.4Ce alloy.

4.4.5 Zener Pinning and Solute Drag

Mg-Zn-Ce precipitates are present throughout the Mg-matrix of each alloy in this study and heavily effect grain boundary velocity and mobility during SRX and grain growth. The common precipitate composition documented in literature is Mg_{12}Ce [36] and/or $Mg_{53}Zn_{45}Ce_2$ [37]. In the solid solution alloy, Mg-4.21 Zn, the only intermetallic compounds possible would be: $Mg_{51}Zn_{20}$, $Mg_{12}Zn_{13}$, Mg_2Zn_3, $MgZn_2$ and/or Mg_2Zn_{11}. In the temperature range of interest, 350-400°C, the most likely precipitate would be $MgZn_2$ [38]. Precipitates cause Zener pinning forces that retard grain boundary motion. Zener pinning forces vary due to both size and phase fraction of precipitates, which is influenced by composition and thermo-mechanical processing. Increases in Zn and/or Ce content generally increase precipitate volume fractions. Due to significantly more Zn content than Ce content, direct correlation between Zn content and SRX kinetics is observed in SRX models.

The faster SRX kinetics of alloys with less Zn content can be accounted for by a decreased amount of fine particle dispersion and resultant solute drag effects. From EDS results, it was determined that Ce is proven to be a solute, in addition to Zn. The maximum solubility of Zn in Mg was reported by Park and Wyman [39] to be 2.5 at.% Zn at 340°C. Rare earth solutes are known to segregate to grain boundaries and strongly affect interface mobility due to solute drag effects [40]. In comparison, elements such as Zn with

smaller atomic radii don't impact interface mobility as significantly as rare-earth solutes do. Boundary pinning by solute drag is less effective in comparison to Zener pinning and is influenced by the boundary nature. Boundary nature could be further explored in future work through analysis of misorientation data via EBSD.

4.5 Conclusions

The initiation of SRX, grain growth kinetics and resultant microstructural characteristics in a set of designed Mg-Zn-Ce alloys were investigated in this study to give further insights into the effect of varying solute and precipitate contents. The following conclusions were determined.

- Increasing Zn content in ZK60 variation Mg-Zn-Ce alloys increases precipitate volume fractions and solute levels present in the matrix, increasing Zener pinning and solute drag, and correspondingly decreasing grain growth kinetics. Increases in Ce content cause more significant decrease of grain growth kinetics, apparently due to greater Mg-Zn-Ce precipitate formation and strengthening.

- Grain growth modeling based on Burke and Turnbull's equation is an accurate way to model grain growth kinetics and the utilization of the Arrhenius equation provides reasonable values for Q, k and k_o for each alloy. These values are included in Table 4.3.

- Texture weakening and texture randomization occurs during SRX in these alloys due to Ce and Zn additions. Basal oriented grains grow preferentially during grain growth, yet rare-earth texture develops at the initiation of SRX within shear bands and grain boundaries. Texture weakening is of significant important in obtaining required mechanical properties for these alloys in industry.

CHAPTER 5

SOLUTE AND PRECIPITATE EFFECTS ON CE-CONTAINING MG ALLOY DYNAMIC RECRYSTALLIZIATION KINETICS

A paper to be submitted to *The Journal of Metallurgical and Materials Transactions A*

Storey, G.K.[1,2]; Sutton, S.[3,4]; McBride, B.N.L[1,5]; Hartman, D.[3,4]; Clarke, A.J.[1,4]; Clarke, K.D.[1,4]

5.1 Abstract

The dynamic recrystallization (DRX) behavior of modified ZK60 alloys is evaluated in this study. The alloy composition variations in precipitate and solute contents can greatly impact DRX behavior and impact microstructure and property development during thermomechanical processing. Calculations of the critical stress required for DRX initiation enables modeling of DRX within industrial processing windows of magnesium alloys. Hot compression tests were carried out from 350-400°C via the Gleeble 3500 thermomechanical simulator at strain rates from 0.001-0.1 s^{-1} to a final strain of 0.8. Microstructural characterization provides further insights into grain size distributions and textures, which are enhanced or retarded by DRX kinetics. A constitutive model shows that increased strain and lower temperatures require greater stress input for DRX to occur. These equations are able to accurately reflect activation energy and effective Zener-pinning effect for each alloy, and can be used to determine industry processing parameters. The flow curves exhibit stages of work hardening, transition, softening and steady state. Texture weakening readily occurs and is observed in the post-DRX microstructure, with greater variations in texture of the high Zn alloys. Texture evolution heavily impacts the properties required in industry processing of Mg-Zn-Ce alloys.

5.2 Introduction

ZK60 alloys are known to have high mechanical strength in comparison to other magnesium alloy grades. Low melting point precipitates, such as Mg_3Zn_7 in Mg-Zn-Zr alloys, cause issues during metallurgical processing. The substitution of rare earth elements, such as Ce, for Zr allows for the formation of higher melting point precipitates, thus improving elevated temperature properties and higher temperature processing windows. Ce additions are also known to enhance corrosion resistance, increase creep resistance, and ultimately speed up DRX [41]. Conventional Mg alloys exhibit improved formability

[1]Center for Advanced Non-Ferrous Structural Alloys (CANFSA), Metallurgical and Materials Engineering Department, Colorado School of Mines, Golden, CO 80401, canfsa.org
[2]Primary researcher and author
[3]Mag Specialties Inc., Denver, CO, 80210
[4]Mentorship and guidance
[5]Assistant to research and theory

at higher temperatures when non-basal slip systems are activated, further facilitating dislocation slip. In this way, DRX is a powerful processing tool to optimize both grain structure and resultant mechanical properties.

After plastic slip is introduced into a material energy accumulates, and the material becomes more thermodynamically unstable. During plastic deformation, DRX process reduces stored energy. Continuous DRX (CDRX) at rotated lattice regions in the area of grain boundaries is the dominant DRX mechanism in magnesium alloys.The CDRX mechanism is known to occur via subgrain rotation during compressive deformation in the temperature range of 250-500°C [42]. There is limited knowledge as to the formation of preferred orientations in magnesium alloys due to other possible deformation mechanisms, such as discontinuous DRX (DDRX) and twin DRX, in certain magnesium alloys [43]. DDRX is a mechanism where previous grain boundaries protrude toward surrounding grains with high dislocation densities, while twin DRX occurs at previously existing twin band intersections or fragments. In alloys with rare earth elements particle-stimulated nucleation (PSN) in the vicinity of second phase particles is common [43]. Texture weaking in Mg alloys has been associated with PSN, as well as other phenomena including particle pinning, solute drag, and heterogeneous deformation, leading to easier shear band formation [44]. Alloying with rare earth elements, such as Ce, can both increase strengthening, ductility and texture weakening of the alloy for a given engineering application.

Modeling the DRX process of magnesium alloys can aid in more efficient processing. Fu et al. studied the DRX mechanisms of Mg-Zn-Mn alloys micro-alloyed with Sm/La/Ca and determined from electron back scatter diffraction (EBSD) that DDRX and PSN mechanisms weakened basal texture [45]. The occurrence of CDRX was observed by Xu et al. in a Mg-13Gd-4Y-2Zn-0.5Zr during compression-torsion deformation at 450°C. It was also determined that the changes in strain rate change the dominant DRX mechanisms [46]. The effect that certain rare earth elements have on alloy properties is highly dependent on the dominant DRX mechanisms that occur.

Calculation of flow stress of hot deformation and DRX can give insight into ideal processing conditions. Flow stress is a parameter that characterizes mechanical properties of a material during hot deformation and is dependent on deformation temperature, strain rate and strain [47]. In modeling strain hardening and DRX during hot deformation, it is essential to investigate both process parameters and deformation mechanisms. There are multiple avenues to model flow stress for hot deformation that have been developed over the years. Holloman developed a mechanical equation at small plastic strains [48]. The next development that considered microstructural evolution and mechanical properties was Mecking and Kocks, who determined that structural parameters, such as dislocation density, can describe DRX flow curves [49]. For magnesium alloys, it is characteristic for flow stress to increase with strain due to work hardening, then

decrease after it reaches the peak due to DRX occurring at a critical strain [47]. This study focuses on analyzing DRX and strain hardening, calculating the critical stress for DRX to occur.

5.3 Experimental Procedures

This section details the experimental procedures regarding DRX studies performed within this research.

5.3.1 Alloy Preparation

The material used for this study is a modified ZK60 (Mg-Zn-Zr) composition, with deliberate variations in Zn levels and a replacement of Ce for Zr in various amounts. This alloy is an extrusion alloy that experiences precipitation hardening and exhibits a finer microstructure after solidification, hot working, or annealing processes. The composition matrix is separated into 3 levels of Zn, varying the hypothesized solute volume, and 3 levels of cerium, varying the hypothesized precipitate volume. The specific experimental alloy compositions are included in Table 5.1.

Table 5.1 Compositional matrix (all in wt.%) for five alloys studied, varied by volume fraction and percent pinning phases.

	Complete solid solution	∼1% pinning phases	∼3% pinning phases
Low solute	˜	LZ-0.4Ce (Mg-1.40Zn-0.38Ce)	˜
Med solute	˜	MZ-0.4Ce (Mg-3.52Zn-0.38Ce)	˜
High solute	HZ-0Ce (Mg-4.21Zn)	HZ-0.1Ce (Mg-5.26Zn-0.12Ce)	HZ-0.3Ce (Mg-6.78Zn-0.31Ce)

The variations in Zn and Ce within these alloys result in changes to second phase insoluble particle types, volume fractions, and distributions. ZK60 is ideally suited for this study, because it is a commercial alloy with insoluble Mg-Zr precipitates that influence DRX kinetics and texture. The samples for this study were machined into small cylindrical compression specimens with dimensions of 10mm in diameter and 15mm in height, where the cylinder height is longitudinal to the extrusion direction.

5.3.2 Thermomechanical Testing

Uniaxial compression tests on the small cylindrical samples for each of the five alloys was conducted on a Gleeble 3500 thermal-mechanical simulator. All samples were compressed to a final true strain of 0.8 and were strained at strain rates of $0.001s^{-1}$, $0.01s^{-1}$ and $0.1s^{-1}$ at either 350 and 400°C. One set of thermocouples was welded on the surface at the half height of each sample and used to monitor temperature throughout the test. The samples were lubricated at the surface of each anvil with layers of Ni paste and grafoil. Each sample was heated up at 5°C/s under force control to the deformation temperature (350°C or 400°C), held in displacement control for 30 s ensuring the temperature throughout the sample

was homogenous, strained to 0.8 true strain and quenched with compressed air. A schematic of the testing procedure is included as Figure 5.1.

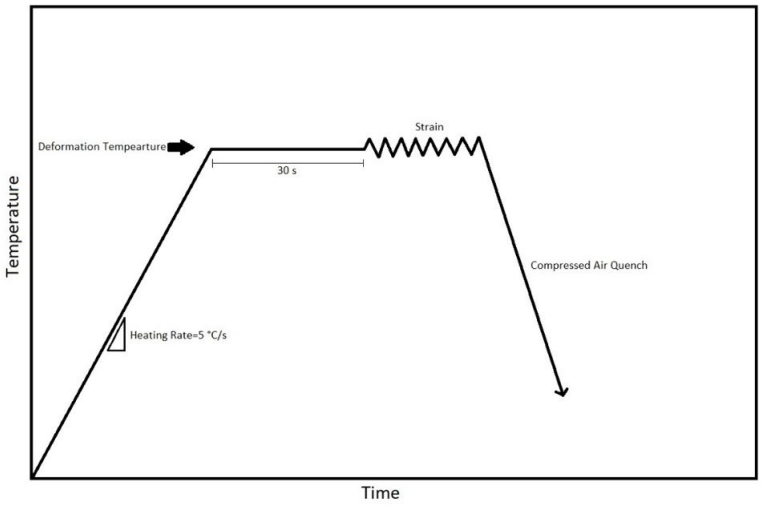

Figure 5.1 Gleeble testing schematic, performed at deformation temperatures of 350°C or 400°C and strain rates of $0.001s^{-1}$, $0.01s^{-1}$ and $0.1s^{-1}$

Load-displacement data was obtained from the compression tests and converted to true stress-true strain using standard conversion equations accounting for cross sectional area changes. This data gives way to analysis of flow behavior and microstructural characterization.

5.4 Results and Discussion

This section details the results obtained from experiments pertaining to DRX studies and discusses findings, relevance and importance of these results.

5.4.1 Flow Curves and Behavior

Force and displacement data was converted to true stress-strain curves for all five alloys tested for all processing conditions. All flow curves are included in Figure 5.2. The flow stress increases to a maximum, then decreases to a steady state when DRX is present. This maximum flow stress is the peak flow stress used through DRX modeling and calculations. At higher strain rates, flow stress increases to a high peak stress, then exhibits moderate work softening. At medium strain rates, flow stress increases to a moderate peak stress, with negligible work softening. At low strain rates, there is a small peak stress and strain, and then negligible work softening. This is characteristic of DRX behavior for magnesium alloys undergoing DRX, because it is characteristic for flow stress to increase to a maximum and then decrease to steady state [47]. A flow stress curve is normally separated by a work-hardening stage, transition stage, softening stage and steady stage. A greater true stress is required for DRX in alloys processed at lower temperatures.

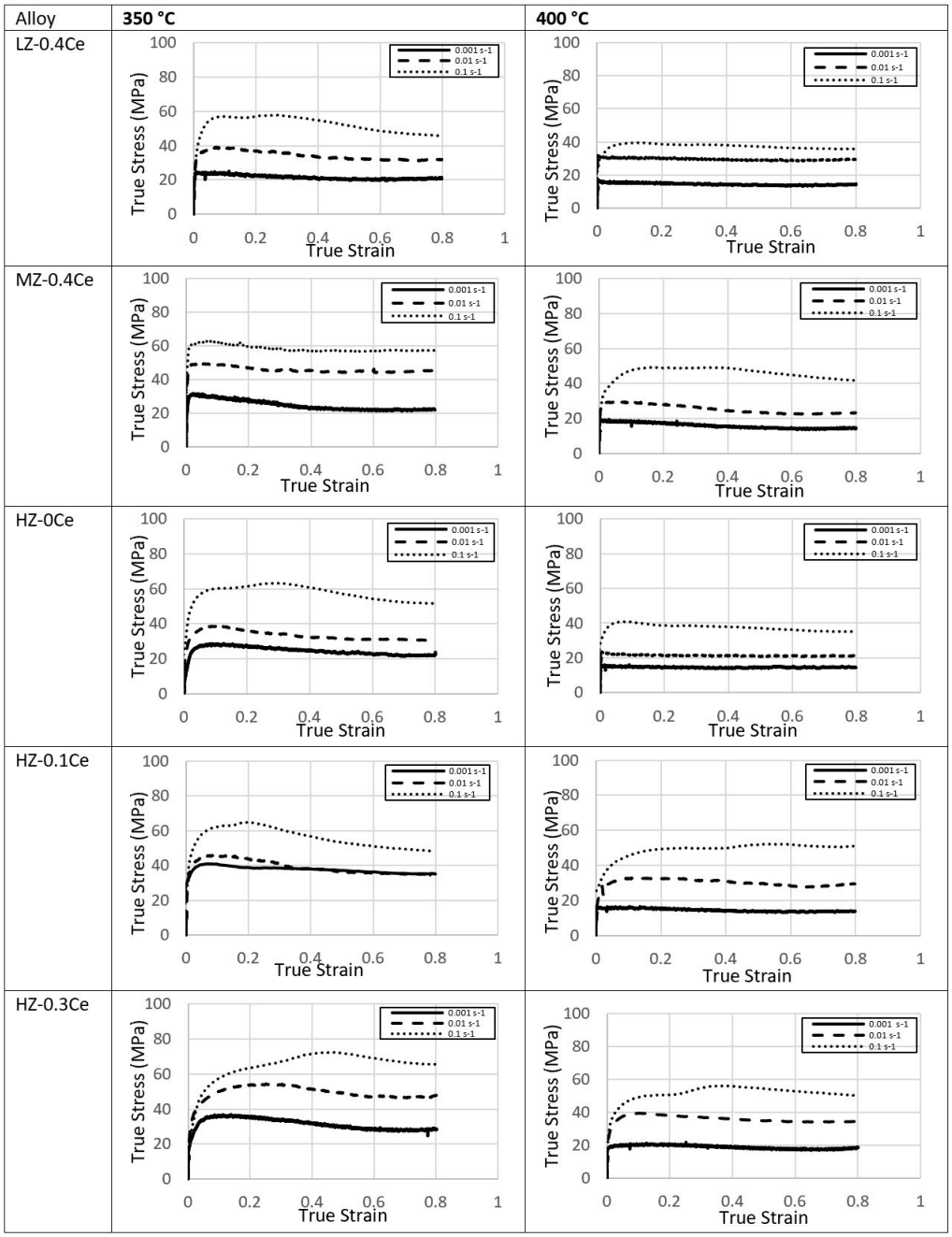

Figure 5.2 Representative flow curves of 5 modified ZK60 alloys varying by both temperature and strain rate.

The onset of DRX can also be identified phenomenologically from the inflection point in the strain hardening rate versus flow curve [49]. The critical stress identified from strain hardening rate graphs identifies the onset of DRX and occurs lower than the peak stress. A third order polynomial, equation 5.1, is fit to each true stress-strain curve up to the peak stress. A third order polynomial effectively fits data

with prolonged and multiple peaks.

$$\theta = A\sigma^3 + B\sigma^2 + C\sigma + D \tag{5.1}$$

where $\theta = d\sigma/d\epsilon$ and constants A, B, C and D allow for calculations of certain DRX conditions. When this equation is differentiated,

$$\frac{\theta}{\sigma} = 3A\sigma^2 + 2B\sigma + C \tag{5.2}$$

The minimum point of this derivative equation correlates to the critical stress. The validity of these equations in comparison to models of expected DRX behavior is confirmed by Najafizadeh et al. in analysis of 304H stainless steel [50]. Calculation of critical stress, according to the derivative goes as follows:

$$\frac{d^2\theta}{d\sigma^2} = 0 = 6A\sigma_c + 2B \tag{5.3}$$

$$\sigma_c = \frac{-B}{3A} \tag{5.4}$$

Each $\frac{\theta}{\sigma}$ polynomial relation and associated σ_{c} are tabulated and utilized to determine the Zener-Hollomon parameter. The activation energy can also be determined by equations for the Zener-Hollomon parameter [51]:

$$\dot{\epsilon} = A_1\sigma_1^n = A_2 exp(\beta\sigma) = A(sinh(\alpha\sigma))^n exp(-\frac{Q}{RT}) \tag{5.5}$$

$$Z = \dot{\epsilon} exp[\frac{Q_d ef}{RT}] = A(sinh(\alpha\sigma))^n \tag{5.6}$$

$$Q_d ef = R[\frac{\partial ln\epsilon}{\partial ln(sinh(\alpha\sigma))}_T][\frac{\partial lnsinh(\alpha\sigma)}{\partial \frac{1}{T}}]_{\dot{\epsilon}} \tag{5.7}$$

where Q_{def} is the deformation activation energy, R is the gas constant (8.314 J/mol K), σ is flow stress, T is the deformation temperature, Z is the Zener-Hollomon parameter, n, A_1, β, A_2, and α are material constants. A graph of peak stress(σ_{p}) for each alloy versus temperature, included as Figure 5.3, displays that increases in Zn content increases σ_{p} that occurs before DRX. The effect of strain rate on σ_{p} was also analyzed, and increases in strain rate require increased σ_{p} during DRX. This increase is relatively linear, due to the direct relationship between σ_{p} and strain rate.

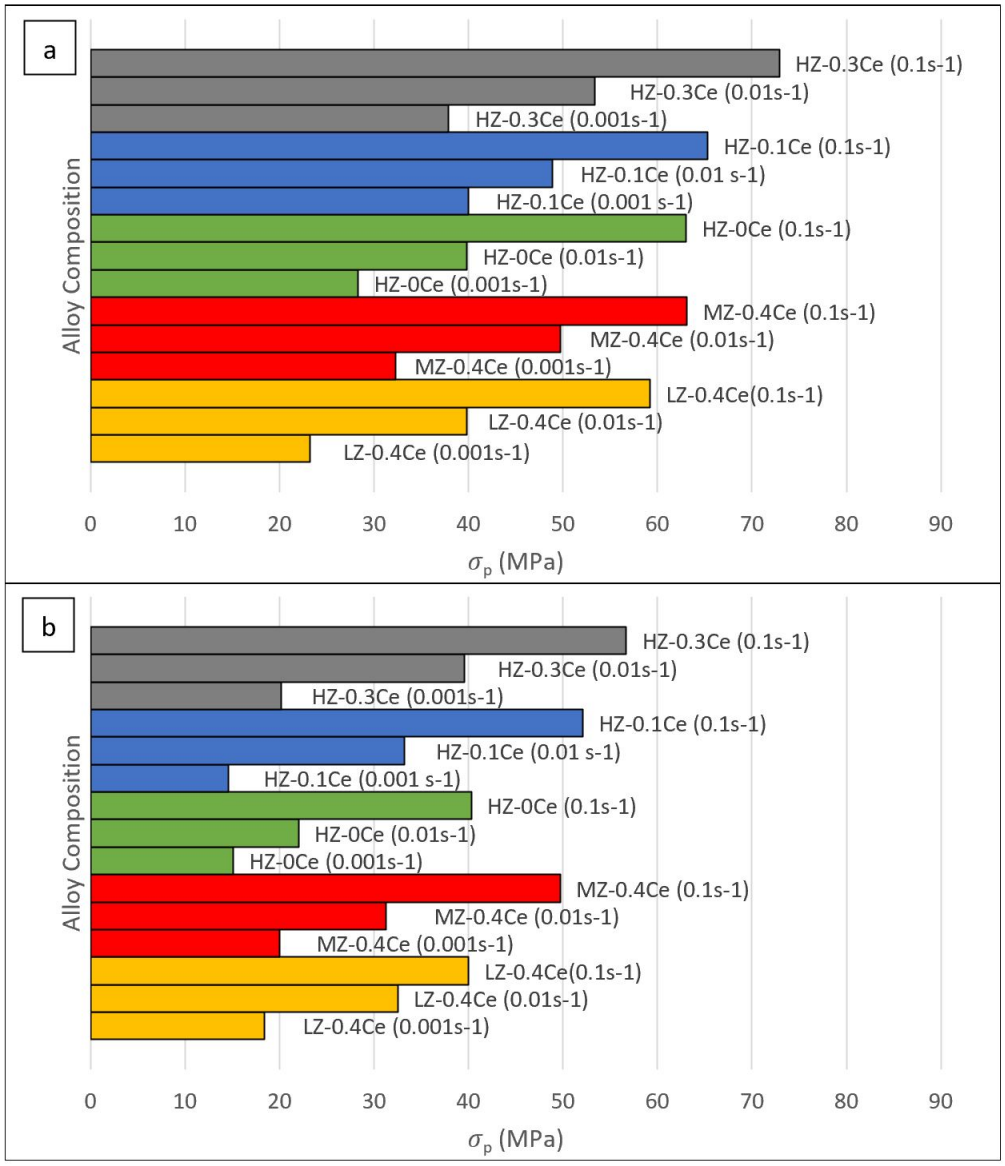

Figure 5.3 Influence of alloy composition on σ_p at 350°C (a) and 400°C (b) of modified Mg-Zn-Ce alloys.

Table 5.2 Tabulated constant values for each alloy composition, organized by alloy and temperature.

Alloy	Temp(°C)	n_1	β	α	n	A
LZ-0.4Ce	350	6.779	0.232	0.034	2.65	9.94
LZ-0.4Ce	400	7.964	0.239	0.030	2.65	9.94
MZ-0.4Ce	350	6.700	0.258	0.038	12.8	2.69
MZ-0.4Ce	400	4.963	0.245	0.049	12.8	2.69
HZ-0Ce	350	6.619	0.169	0.026	9.60	183
HZ-0Ce	400	4.005	0.221	0.055	9.60	183
HZ-0.1Ce	350	4.429	0.205	0.046	6.00	7.42E3
HZ-0.1Ce	400	4.031	0.230	0.057	6.00	7.42E3
HZ-0.3Ce	350	10.670	0.257	0.024	2.87	2.87E12
HZ-0.3Ce	400	4.929	0.321	0.065	2.87	2.87E12

The value of n_1 is obtained from the linear regression of ln$\dot{\epsilon}$-σ_p using equation 5.7 [11]. The values of β are derived from the slope of the linear regression of ln$\dot{\epsilon}$-$ln\sigma_p$. The values of n_1, β and α values ($\alpha = \beta/n_1$) are included in Table 5.2.

From these values, it is essential to calculate activation energy, Q, for DRX. The linear slope of $ln\epsilon vs. ln[sinh(\alpha\sigma)]$, varied by temperature, is the left side of equation 5.7. The linear slope of ln[sinh($\alpha\sigma$)] vs. 1/T at different strain rates is the right side of equation 5.7. The Q value for each $\dot{\epsilon}$ and T is calculated to further determine Z values, included as ln(Z) values in Table B.1, included in the Appendix. Table B.1 also includes the strain hardening-stress relation, calculated critical stress and peak stress values. These Q values at each strain rate are included in Figure 5.4. Q increases with Zn content, and similarly but to a lesser degree with Ce content. The average Q for the LZ-0.4Ce alloy is 81.9% less than the average Q for the HZ-0.3Ce alloy. The average Q for HZ-0Ce is 69.5% less than the average Q for HZ-0.3Ce.

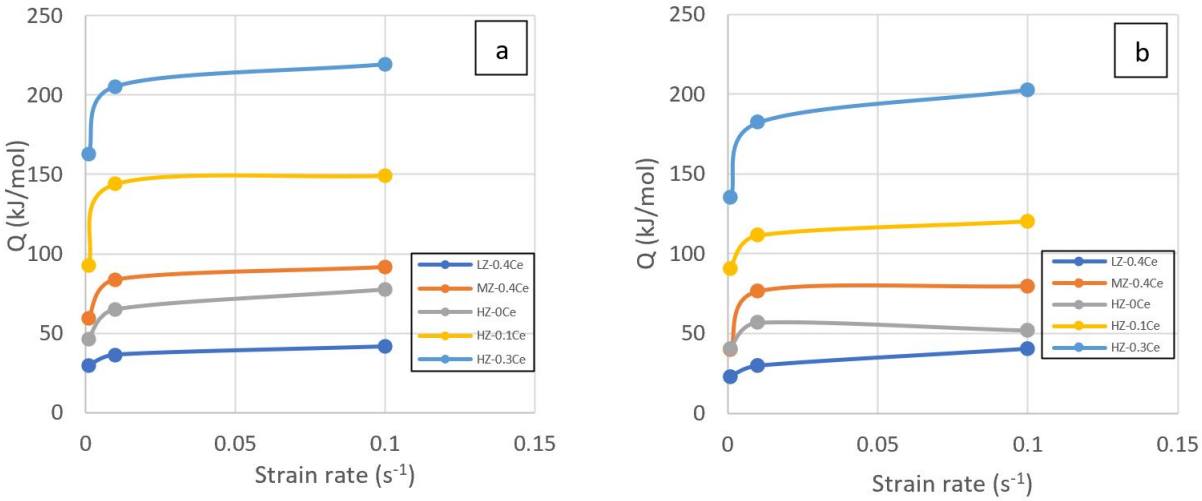

Figure 5.4 Calculated Q values-strain rate at 350°C (a) and 400°C (b).

Z values are calculated based on $\dot{\epsilon}$, Q, R and T of each, as set up in equation 5.4. This Zener-Hollomon parameter describes the effect of both strain rate and temperature on flow stress of materials. For magnesium alloys there is known to be a linear relationship between flow stress and the Zener-Hollomon parameter [51]. The linear relationship for each alloy is determined and displayed in Figure 5.5, and was utilized to determine a constitutive equation describing DRX kinetics.

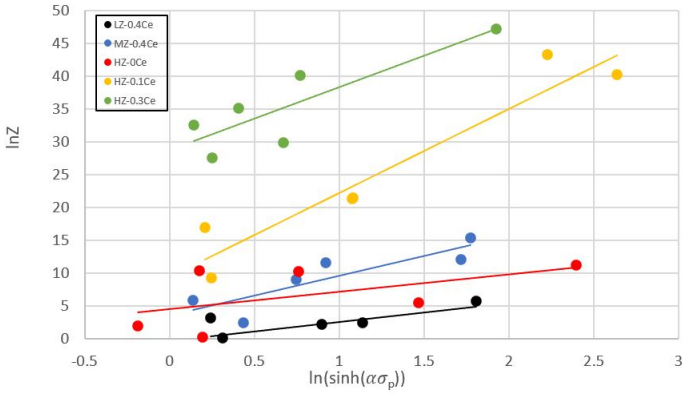

Figure 5.5 Relationship of flow stress and the Zener-Hollomon parameter at each processing condition. The linear regression of each alloy dataset provides the stress exponent, n, and constant A.

The stress exponent (n) and constant A are determined from the linear regression of each dataset and are included in Table 5.3. The constitutive equation can be modeled using tabulated values in the format:

$$\sigma_p = \frac{1}{\alpha}((\frac{Z}{A}^{\frac{1}{n}}) + (\frac{Z}{A}^{\frac{2}{n}}) + 1)^{\frac{1}{2}} \tag{5.8}$$

An additional relation between Z and σ_p based on the linear regression of the two is determined for each alloy, accounting for the stress exponent, n, and constant A. These values can also be found in Table 5.2. The accuracy of this modeling method has been deemed accurate for magnesium alloys, specifically a T-4 treated ZK60 magnesium alloy by Yu et al. [51]. The model is more varied for samples processed at higher strain rates and lower temperatures, meaning that DRX processes are less controlled under these conditions and should be avoided in industrial processing. Samples with higher Zn contents, as well as higher Ce contents, have slower DRX and require more energy for the process to begin.

Table 5.3 Function of Zener-Hollomon parameter (Z) and flow stress (σ_p) as a linear regression equation for each alloy. The slope represents stress exponent, n, and the intercept is constant A.

Alloy	lnZ-ln(sinh($\alpha\sigma_p$))
LZ-0.4Ce	LnZ=2.8711ln(sinh($\alpha\sigma_p$))-0.2696
MZ-0.4Ce	LnZ=6.0024ln(sinh($\alpha\sigma_p$))+3.6255
HZ-0Ce	LnZ=9.6003ln(sinh($\alpha\sigma_p$))+28.687
HZ-0.1Ce	LnZ=12.766ln(sinh($\alpha\sigma_p$))+9.4806
HZ-0.3Ce	LnZ=2.6505ln(sinh($\alpha\sigma_p$))+4.4968

5.4.2 Microstructural Characterization

Electron backscatter diffraction (EBSD) was completed on all alloys and processing conditions. After compression testing, each sample was mounted, ground, polished to 0.05µm colloidal silica and etched after each polishing step in a solution of 4.2g picric acid, 70 mL ethanol, 10mL glacier acetic acid, and 10mL deionized water, for 10 s [52]. The polished surface for these samples is longitudinal to the compression direction. EBSD mapping analysis was performed with a 20kV electron beam, 18mm working distance, and 2µm step size. Each inverse pole figure (IPF) map was processed with Neighbor Pattern Averaging Indexing (NPAR) in Orientation Imaging Microscopy (OIM) software. Representative IPF maps for each condition are included in Figure 5.6.

Texture weakening is observed after DRX. The basal texture weakens, and the non-basal texture is preferential, with the exception of some basal areas throughout the sample. This can be observed easily in the IPF maps where blue and green colors are non-basal, and red and warmer colors are near-basal/basal orientations. There are some long, elongated unrecrystallized grains in certain areas where DRX did not occur. Many of these grains were near-basal oriented, potentially due to less slip in these regions. Zener pinning and solute drag have an effect on how significantly DRX occurs throughout the microstructure, and increased amounts of Zn and Ce cause less homogenous post-DRX texture, due to areas with previously in-homogeneous solute distribution. This observance is particularly prevalent in the HZ-0.3Ce and HZ-0.1 Ce alloys. An increase in strain in these compression tests, especially at lower temperatures, causes increased inhomogeneous texture.

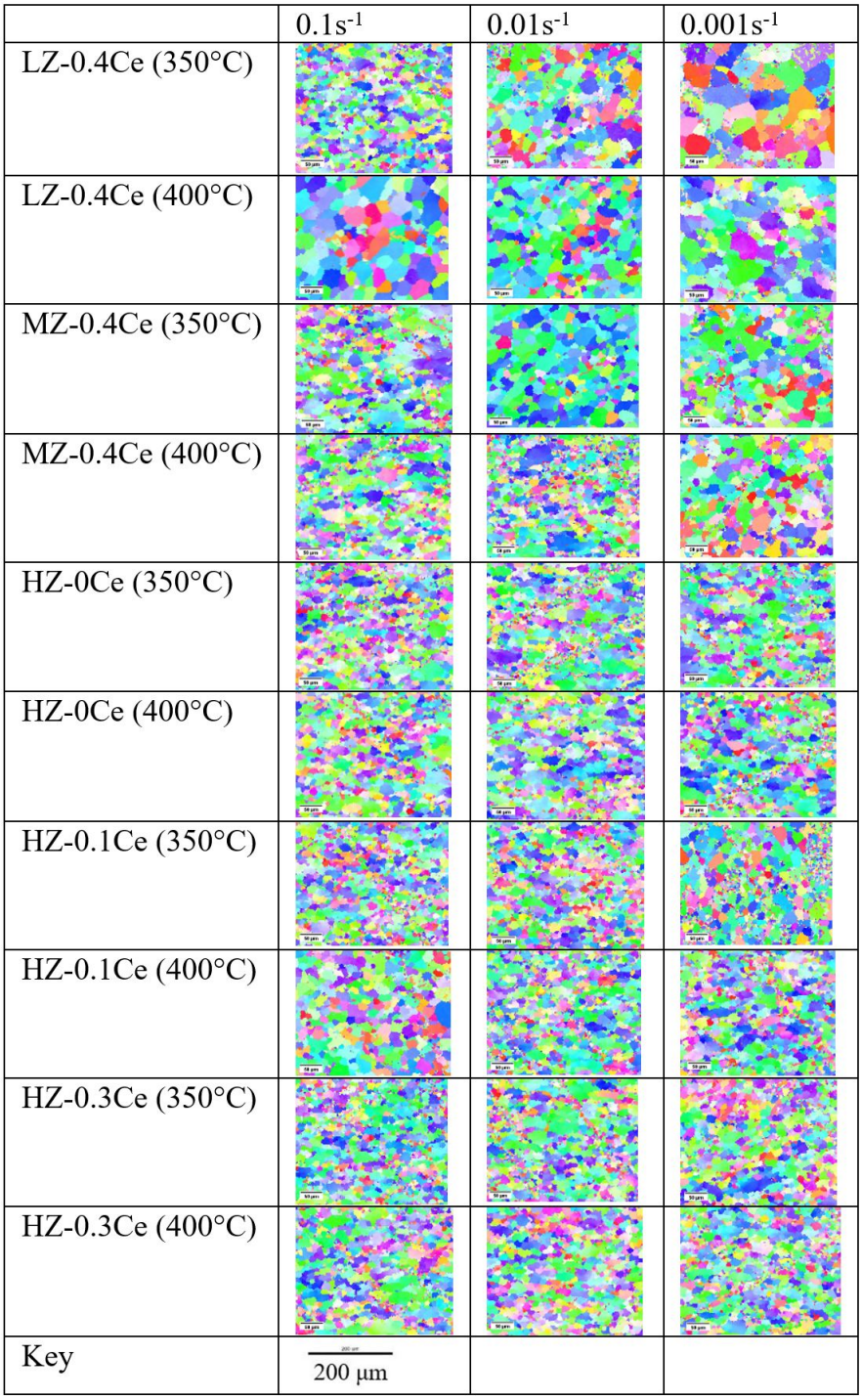

Figure 5.6 Representative IPF maps at strain rates $0.1s^{-1}$-$0.001s^{-1}$ and 350°C/400°C, with 50µm scale bar. IPFs were developed for each alloy and processing condition.

5.5 Conclusions

The DRX kinetics during compression testing at elevated temperatures and resultant microstructural properties in a set of designed Mg-Zn-Ce alloys were investigated in this study to give further insights into the effect of varying solute and precipitate contents. The following conclusions were determined.

- Ce additions impede DRX kinetics to a greater extent than Zn additions, per wt% increase. Ce additions dramatically increase precipitate fractions and Zener pinning, while Zn additions primarily increase solute drag. Zener pinning, by this reasoning, has a greater impact on retarding DRX kinetics than solute drag. The Q is lowest for the HZ-0Ce alloy, yet highest for the HZ-0.3Ce alloy because of this.

- The determined constitutive equations for the DRX process accurately reflect the activation energy and effective Zener-pinning effect expressed in each alloy and can be used to determine industrial processing parameters given different processing conditions.

- The σ_p, determined via flow curves, and σ_c, determined through calculations, are an accurate representation of DRX initiation. Q and σ_p are directly correlated, and σ_p is greater for alloys with greater Ce additions and Zn contents. Greater dependence on Ce additions is observed than for Zn additions.

- Texture weakening and randomization is prevalent in the microstructure after DRX. A less homogeneous basal texture is observed with increases in Zn, higher strain rates and lower temperatures.

CHAPTER 6
SUMMARY AND CONCLUSIONS

This study aimed at determining how variations in composition, and associated precipitate volume fractions, influence SRX, grain growth and DRX kinetics. This study also focused on the softening effects experienced through SRX and grain growth, as well as texture evolution. The static annealing temperatures and deformation temperatures were between 350°C-400°C. This temperature range is the common hot working and extrusion range for Mg-Zn-RE alloys in industry.

A sample of each alloy composition was statically heat treated from 6-60 h, then microstructural characterization and hardness testing were conducted on each condition. Grain size decreased until about 10 h for all alloys, when SRX concludes. Grain size continually increases thereafter until 60 h, due to grain growth. Softening occurs through both SRX and grain growth, yet at a faster rate during grain growth due to large increases in grain size. During SRX, texture weakening and randomization occur where non-basal grains preferentially nucleate starting in the vicinity of shear bands and grain boundaries. The nature of this non-basal orientation gives insight into anticipated ductility of these alloys in engineering application. Basal grains are then the preferential orientation for grain growth, due to the initial texture of as-received samples and previous processing history.

There is a significant effect of Ce and Zn additions on the kinetics of SRX and grain growth. Ce additions, per wt%, are more effective than Zn additions at impeding SRX and grain growth kinetics. This is due to coarse, hard Mg-Zn-Ce precipitates that develop within each condition that cause precipitate hardening and slow grain boundary motion. Zn additions contribute to the solute amount and distribution within the Mg-matrix. These solutes cause solute drag and decrease grain boundary motion, but at a lesser extent than precipitates in these alloys. Grain growth modeling based on Burke and Turnbull's equation further define the effect of precipitate and solute amount on grain growth kinetics through determination of Q values and equations for the average grain size growth based on time and temperature.

In order to study DRX kinetics of these alloys, thermomechanical testing was conducted via compression at various strain rates at 350°C and 400°C. This force-displacement data was used to determine flow curves for each processing condition and alloy. Constitutive equations were developed to accurately reflect the Q and Z values, taking into account peak stress and calculated critical stress values. These values determine to what extent precipitate and solute amounts within each alloy affect DRX kinetics. These models can be easily implemented in industrial processing of these alloys to make informed processing decisions. Microstructural characterization was conducted to analyze texture. Texture

weakening and randomization are heavily prevalent in the post-DRX microstructures. Texture weakening is observed as less red coloration is observed in IPF maps. Texture weakening through SRX and DRX causes more advantageous mechanical properties within Mg-RE alloys. Less homogeneous texture, with greater basal texture, was observed for alloys with higher Zn contents, at higher strain rates and lower temperatures. Increases in Ce have a more dramatic effect than Zn additions on Q values, as well as more dramatic texture evolution. Zener-pinning parameter values increase as Zn amounts increase and correlate to peak stress observed in the flow curves. These observations allow for more informed texture control and alloy design in the future.

CHAPTER 7

FUTURE WORK

There is a multitude of additional research that could be conducted on Mg-Zn-RE alloys in the future to further understand and control the industrial processing of these alloys. Based on the findings of this research, there are some specific steps that could be taken to further the understanding of this alloy system. In order to further develop a SRX model, static heat treatments could be conducted at a smaller time or lower temperature range. Suggested by this data, intervals starting under 1 h up to 10 h would be effective. Misorientation data, grain-to-grain, within this time range would assist to further explain texture weakening occuring during SRX. Kernel Average Misorientation (KAM) data on each of these processing conditions would also give information about low angle and high angle boundary evolution. Grain growth kinetics could also further be evaluated by tracking texture components at each annealing condition and comparing this data to the crystal orientation to determine the preferred grain orientation that grows as grain growth progresses. Throughout this research, comparing alike regions during microstructural characterization was essential, due to inhomogeneous texture and internal strains that can develop during extrusion. Bulk texture evaluation from center-to-edge of an extrusion using x-ray diffraction (XRD) or neutron diffraction might prove to be helpful in the future. There is still so much to be explored and understood in Mg-RE alloys.

REFERENCES

[1] Bettles, C. Barnett, M., Advances in wrought magnesium alloys, Woodhead Publishing, 2012.

[2] Bhattacharjee, T., Sasaki, T., Suh, B., Role of Zr in the Microstructure Evolution in Mg-Zn-Zr Based Wrought Alloys, Magnesium Technology, (2015), 1-16.

[3] Sheikhani, A. and Palizdar, Y., The effect of Ce addition (up to 3%) and extrusion ratio on the microstructure and tensile properties of ZK60 Mg alloy, IOP Publishing, Materials Research Express, (2019).

[4] ASTM Standard: B91-17, Standard Specification for Magnesium-Alloy Forgings, ASTM International.

[5] ASTM Standard: B107/B107M-13, Standard Specification for Magnesium-Alloy Extruded Bars, Rods, Profiles, Tubes, and Wires, ASTM International.

[6] Kim, J. and Kawamura, Y., Effect of the Extrusion Conditions on the Microstructural and Mechanical Properties of Indirect extruded Mg-Zn-Y Alloy with LPSO Phase, Magnesium Technology TMS, (2013).

[7] Robson, J.D, Haigh, S.J., David, B., and Griffiths, D. Grain Boundary Segregation of Rare-Earth Elements in Magnesium Alloys. Metallurgical and Materials Transactions A, (2016), 47, 522-530.

[8] Alaneme, K. K, Oketete, E. A., Recrystallization mechanisms and microstructure development in emerging metallic materials: A review., Journal of Science: Advanced Materials and Devices, (2018).

[9] Burke, J.E Turnbull, D., Recrystallization and grain growth, Prog. Met. Phys. (1952), 220-292.

[10] Cahn, R. W, A new theory of recrystallization nuclei, Proc. Phys. Soc., (1950), 323-336.

[11] Cottrell, A.H., Theory of Dislocations, Progress in Metal Physics. Vol 4, Pergamon Press, London, (1953) 251-255.

[12] Huphreys, F.J., Nucleation in recrystallization, Mater. Sci. Forum, (2004) 467-470.

[13] Alaneme, K.K., Phase transformation studies of a low alloy steel in the (a+γ) phase region. Material Res, (2010), 13 (1), 113-117.

[14] Nie, JF. Precipitation and Hardening in Magnesium Alloys, Metallurgical and Materials Transactions A., (2012), 43, 3891-3939.

[15] Zhang, Y., Jiang, H., Wang, Y., Xu, Z., Effects of Second-Phase Particles on Microstructure Evolution of Mg-2Zn Based Magnesium Alloys during Annealing Treatment, Metals, (2020), 10(6), 777.

[16] Biesiekierski, A., Li, Y., Wen, C., The Application of the Rare Earths to Magnesium and Titanium Metallurgy in Australia, Advaned Materials, (2019), 32 (18).

[17] Wang, N., Ji, Y., Wang, Y, et.al, Two Modes of Grain Boundary Pinning by Coherent Preciptiates, Acta Materialia, (2017), 135-C.

[18] Zhang, Y., Jiang, H., Kang, Q., et.al, Microstructure evolution and mechanical property of Mg-3Al alloys with addition of Ca and Gd during rolling and annealing process, Journal of Magnesium and Alloys, (2020), 8-3, 769-779.

[19] Xiya, F., Danquing, Y., Wenhai, L., et.al., Effects of yttrium on recrystallization and grain growth of Mg-4.9Zn-0.7Zr alloy, Journal of Rare Earths, (2008), 26-3.

[20] Mouhib, F-Z., Sheng, F., Mandia, R., et.al., Texture Selection Mechanisms during Recrystallization and grain Growth of a Magnesium-Erbium-Zinc Alloy, Metals, (2021), 11-1.

[21] Galiyev, A., Kaibysev R. Gottstei, G., Correlation of Plastic Deformation and Dynamic Recrystallization in Magnesium Alloy ZK60, Acta Materialia, (2001), (49) 1199-1207.

[22] Kaibyshev, R. O. Sitdikov, O. S., Introduction to the Physical Metallurgy of Welding, Physical Metallurgy. 1992, 73-420.

[23] Gottstein, G. Kocks, U.F., Thermo-Mechanical Processing of Metallic Materials, Material Science Technology., (1991), 7-158.

[24] Ion, S.E., Humphreys, F.J. White, S.H., The Effect of Equal Channel Angular Pressing Process on The Microstructure of AZ31 Mg Alloy Strip Shaped Specimens, Acta Materialia, (1982), 145-149.

[25] Jiang, M.G., Xu, C., Yan, H., et.al., Correlation between dynamic recrystallization and formation of rare earth texture in a Mg-Zn-Gd magnesium alloy during extrusion, Scientific Reports, (2018),8-16800.

[26] Jin, L., Mirshra, R.K., Sachdev, A.K., Texture Modification During Extrusion of Some Mg Alloys, Metallurgical and Materials Transactions A, (2012), (43) 2148-2157.

[27] Li, Lu., Wang, Y., Li, H., et.al., Effect of the Zener-Hollomon parameter on the dynamic recrystallization kinetics of Mg-Zn-Zr-Yb magnesium alloy, Computational Materials Science, (2019), 166, 221-229.

[28] Wang, S., Kang, S.B. Cho, J., Effect of hot compression and annealing on microstructure evolution of ZK60 magnesium alloys. J Mater Sci 44, (2009), 5475–5484.

[29] Stanford, N. Barnett, M.R., The origin of "rare earth" texture development in extruded Mg-based alloys and its effect on tensile ductility", Materials Science and Engineering; A, (2008), (496)(1-2), 299-408.

[30] Chapman, J.A. Wilson, D.V. Journal of the Institute of Metals, (1962), (91)39.

[31] Yu, H., Kim, Y.M., You, B.S., Yu, H.S. Park, S.H., Effects of cerium addition on the microstructure, mechanical properties and hot workability of ZK60 alloy, Mater. Sci. Eng. A (2013), (559) 798–807.

[32] Silva, E.P., Buzolin, R.H., Marques, F., Soldera, F., Alfaro, U. Pinto, H.C. Journal of Magnesium and Alloys, (2002).

[33] Gao, X., He, S.M., Zeng, X.Q., Peng, L.M., Ding, W.J. Nie, J.F., Materials Science and Enginering: A, (2006), (431)(1-2), 322-37.

[34] Hadorn, J.P., Hantzsche, K., Yi, S. , Bohlen, J., Letzig, D. Agnew, S.R., Met. and Mat. Trans A, (2012), (43A), 1363-75.

[35] Ball, E.A. Prangnell, P.B., Scripta Metall. Mater., (1994), (31) , 111–16.

[36] Schmid-Fetzer, R. Grobner, J., Thermodynamic Database for Mg Alloys–Process in Multicomponent Modeling, Institute of Metallurgy, Clausthal University of Technology, (2012).

[37] Sheikhani, A. Palizdar, Y., The effect of Ce addition (up to 3%) and extrusion ratio on the microstructure and tensile properties of ZK60 Mg alloy, IOP Publishing Ltd, (2019).

[38] Mezbahul-Islam, M., Mostafa, A.O. Madraj, M., Essential Magnesium Alloys Binary Phase Diagrams and Their Thermochemical Data, Hindawi, (2014).

[39] Park, J.J. Wyman, L.L., Phase relationships in magnesium alloys, WADC technical Report: Astia, (1957).

[40] Pei, R., Zou, Y., Wei, Q., Al-Samman, T., Acta Materialia, (2021), (208).

[41] Silva, E.P. Pinto, H.C., Effect of Ce-base mischmetal addition on the microstructure and mechanical properties of hot-rolled ZK60 alloy, Journal of Magnesium and Alloys, (2020).

[42] Roodposhti, S., Sarkar, K.L, Murty, H. Brody, R, Scattergood, R., Grain boundary sliding mechanism during high temperature deformation of AZ31 magnesium alloy, Mater.Sci.Eng.A, (2016), (669), 171-177.

[43] Fatemi, S.M Paul, H., Characterization of continuous dynamic recrystallization in WE43 magnesium alloy, Materials Chemistry and Physics, (2020), (257).

[44] Dong, J., Sun, J., Jin, L., Zhang, Z., Ding, W., Texture evolution in Mg-Al and Mg-RE alloy during hot extrusion, 135h International Conference on Fracture, (2013).

[45] Fu, L., Le, Q., Hu, W., Zhang, J., Wang, J., Strengths and Ductility Enhanced by Micro-Alloying Sm/La/Ca to Mg-0.5Zn-0.2Mn Alloy, Journal of Materials Research and Technology, (2020), (9-3), 6834-6849.

[46] Xu, P., Yu, J. Zhang, Z., Microstructure and texture Evolution of Mg-Gd-Y-Zn-Zr Alloy by Compression-Torsion Deformation, Materials, (2019), 12-17.

[47] Liu, J., Cui, Z. Li, C., Modelling of flow stress characterizing dynamic recrystallization for magnesium alloy AZ31B, Computational Materials Science, (2008), 41-3, 375-382.

[48] Hollomon, J.H., The mechanical equation of state [J]., Trans AIME, (1947), 171, 535-545.

[49] Mecking, H. Kocks, U.F., Kinetics of flow and strain-hardening [J]., Acta Metallurgica, (1981), 29-11, 1865-1875.

[50] Najafizadeh, A. Jonas, J., Predicting the Critical Stress for Initiation of Dynamic Recrystallization, ISIJ International, (2006), 46-11, 1679-1684.

[51] Yu, H., Yu, H., Min, G., Park, S., You, B., Kim, Y., Strain-Dependent Constitutive Analysis of Hot Deformation and Hot Workability of T4-Treated ZK60 Magnesium Alloy, Met. Mater.Int, (2013), 19-4, 651-665.

[52] Lin, T., Zhou, J.X., Jing, Y.T, Zhang, L.L, Meng, X.B., Improving mechanical properties of ZK60 magnesium alloy by cryogenic treatment before hot extrusion, Dr Gruyter, (2020).

[53] Yuan, Y., Ma, M., Jiang, J., High Mechanical Properties of Rolled ZK60 Mg Alloy through Pre-Equal Channel Angular Pressing, Mechanika, (2016), 256-259.

APPENDIX A
COPYRIGHT APPROVALS

Previous approval for Figure 2.1 [21] was granted for inclusion in this thesis. The details of this approval are included below as the terms and conditions document provided by Elsevier via email correspondence.

Aug 13, 2021
This Agreement between Colorado School of Mines – Gillian Storey ("You") and Elsevier("Elsevier") consists of your license details and the terms and conditions provided by Elsevier and Copyright Clearance Center.
License Number 5126860079192 License date Aug 13, 2021 Licensed Content Publisher Elsevier Licensed Content Publication Acta Materialia Licensed Content Title Correlation of plastic deformation and dynamic recrystallization in magnesium alloy ZK60 Licensed Content Author A Galiyev,R Kaibyshev,G Gottstein Licensed Content Date Apr 19, 2001 Licensed Content Volume 49 Licensed Content Issue 7 Licensed Content Pages 9 Start Page 1199 End Page 1207
Type of Use reuse in a thesis/dissertation Portion figures/tables/illustrations
Number of figures/tables/illustrations 1 Format electronic
Are you the author of this Elsevier article? No
Will you be translating? No
Title Solute and Precipitate Effects on Magnesium Recrystallization and Grain Growth
Institution name Colorado School of Mines Expected presentation date Sep 2021
Portions Figure 1
Requestor Location
Colorado School of Mines
1500 Illinois St
GOLDEN, CO 80401
United States
Attn: Center for Advanced Non-Ferrous Structural Alloys

APPENDIX B
SUPPLEMENTARY TABLE B.1

This section includes the table referenced in Chapter 5 on page 39. The table is included as a full-size horizontal table on the next page.

Table B.1 Critical stress and third order polynomial descriptions of strain hardening rate versus stress, calculated values of Q and Z for each T and strain rate. Further explained in Chapter 5, page 39.

Alloy	Temp(°C)	Strain Rate(s^{-1})	Strain hardening rate/stress relation	Critical stress (MPa)	Peak stress (MPa)	Q(kJ/mol)	$ln(Z)$
LZ-0.4Ce	350	0.001	y=-2E6+06x^3+46935x^2+426.22x+14.491	19.7	23.2	29.51	-1.21
	400	0.001	y=-7926.9x^3+835.11x^2+69.716x+14.023	17.2	18.4	23.02	0.15
	350	0.01	y=-4731.7x^3+1214.3x^2+166.69x+15.349	35.5	39.8	36.42	2.42
	400	0.01	y=-441803x^3+28292x^2+219.75x+13.044	26.3	32.5	29.83	3.21
	350	0.1	y=-2715.2x^3+1285.7x^2+68.162x+13.561	45.7	59.2	41.61	5.73
	400	0.1	y=-7818.6x^3+2236.5x^2+90.106x+13.683	35.8	40.0	40.29	2.16
MZ-0.4Ce	350	0.001	y=-253943x^3+15676x^2+579.38x+4.1728	30.5	32.3	59.32	2.41
	400	0.001	y=-619280x^3+19041x^2+177.17x+12.985	16.1	20.0	39.52	5.84
	350	0.01	y=-54045x^3+6422.4x^2+577.35x+19.167	48.8	49.7	83.63	11.54
	400	0.01	y=-355510x^3+4504.5x^2+218.7x+13.233	27.9	31.3	76.29	9.03
	350	0.1	y=-9020.2x^3+2465.7x^2+358.55x+14.04	60.4	63.1	91.49	12.04
	400	0.1	y=-696.34x^3+186.82x^2+248.47x+14.082	34.3	49.7	79.46	15.32
HZ-0Ce	350	0.001	y=-53483x^3+5321.6x^2+225.27x+14.462	25.8	28.3	46.27	2.02
	400	0.001	y=420.95x^3-351.07x^2+55.073x+13.431	11.1	15.1	40.29	0.29
	350	0.01	y=-7222.5x^3+2059.5x^2+105.07x+13.691	36.1	39.8	65.14	10.39
	400	0.01	y=112285x^3+2925.2x^2+18.841x+19.944	19.9	22.0	56.49	5.49
	350	0.1	y=-28487x^3+5803.5x^2+429.39x+13.638	60.6	63.1	77.7	10.27
	400	0.1	y=-69077x^3+8817.6x^2+313.02x+13.177	37.1	40.3	51.65	6.93
HZ-0.1Ce	350	0.001	y=203.3x^3-256.25x^2+126.98x+14.958	38.2	40.2	92.56	16.96
	400	0.001	y=2000000x^3-17240x^2-82.32x+12.696	12.4	14.6	90.57	9.28
	350	0.01	y=2085.9x^3-695.45x^2+69.416x+28.418	30.4	48.9	143.98	21.42
	400	0.01	y=-49734x^3+31536x^2+238.77x+12.849	27.3	33.2	111.19	21.30
	350	0.1	y=-29305x^3+5938.3x^2+401.79x+13.683	58.9	65.3	149.27	43.21
	400	0.1	y=-71421x^3+10194x^2+371.096x+12.766	45.8	52.1	120.18	40.15
HZ-0.3Ce	350	0.001	y=-28821x^3+5266x^2+121.97x+10.871	37.0	37.9	162.65	32.51
	400	0.001	y=2645.3x^3-756.5x^2+64.241x+25.828	18.0	20.2	135.52	27.53
	350	0.01	y=-39002x^3+4581.5x^2+422.4x+25.828	47.1	53.4	205.42	35.04
	400	0.01	y=-286629x^3+16718x^2+244.12x+23.371	32.3	39.6	182.11	29.82
	350	0.1	y=-457432x^3+66944x^2+338.13x+38.477	70.6	72.9	219.28	40.04
	400	0.1	y=-201765x^3+48346x^2+158.06x+12.891	56.5	56.7	202.65	47.20